The Astrophysical Journal, 822:8 (23pp), 2016 May 1 doi:10.3847/0004-637X/822/1/8

EFFECT OF PERCHLORATES ON ELECTRON RADIOLYSIS OF GLYCINE WITH APPLICATION TO MARS

Sándor Góbi[1,2], Matthew J. Abplanalp[1,2], and Ralf I. Kaiser[1,2]
[1] Department of Chemistry, University of Hawaii at Mānoa, Honolulu, HI 96822, USA; ralfk@hawaii.edu
[2] W. M. Keck Laboratory in Astrochemistry, University of Hawaii at Mānoa, Honolulu, HI 96822, USA
Received 2015 October 28; accepted 2016 January 14; published 2016 April 26

ABSTRACT

This work explores the radiolytic decomposition of glycine (H_2NCH_2COOH) under simulated Martian conditions in the presence of perchlorates (ClO_4^-), which are abundant oxidizers on the surface of Mars, by energetic electrons at 10, 160, 210, and 260 K, mimicking the radiation exposure of the Martian regolith in the first 5–10 cm depths over about 250 million years. Our experiments present quantitative evidence that the rate constants of the glycine decomposition in the presence of magnesium perchlorate hexahydrate ($Mg(ClO_4)_2 \cdot 6H_2O$) were a factor of about two higher than that of the pure glycine, suggesting that energetic oxygen atoms (O) released from the ClO_4^- have a significant effect on the decomposition rates and accelerate them by providing a unique oxidizing environment in the radiolyzed samples. Hence, two decay mechanisms exist: radiolysis by the electrons and oxidation by the O atoms. Within the Mars-relevant temperature range covering 160–260 K, the destruction rates are nearly temperature invariant with rates varying as little as 5%. Further, the formation rates of carbon dioxide (CO_2) and carbon monoxide (CO) are both accelerated in the presence of ClO_4^- by a factor of three to five, supporting our conclusion of an active oxygen-initiated chemistry. In addition, the degradation rates are significantly higher than the formation rates of CO_2 and CO. This suggests that, besides the decarboxylation, alternative degradation pathways such as a polymerization of glycine must exist. Finally, besides CO_2 and CO, three alternative products were identified tentatively: methylamine (CH_3NH_2), methane (CH_4), and ammonia (NH_3).

Key words: astrochemistry – methods: laboratory: solid state – planets and satellites: surfaces – techniques: spectroscopic

1. INTRODUCTION

An understanding of the physicochemical processes and fate of organics on the surface of Mars is of primary importance to the planetary science and astrobiology communities. Organic matter can be accumulated on the surface of Mars through either in situ formation (Hubbard et al. 1971) or exogenous delivery via interplanetary dust (Flynn 1996; Moores & Schuerger 2012) and meteorite particles (Botta & Bada 2002). Flynn proposed that these processes deliver up to 10^8 g per year of reduced carbon species to Mars (Flynn 1996, 1997). Ten Kate et al. (2005) pointed out that based on the abundances of amino acids in meteorites at the level of 5–60 ppm, an annual influx to the Martian surface of 15 ng m^{-2} yr^{-1} should yield detectable concentrations in the ppb range in a relatively short time period of only 1000 yr. Additionally, due to the thin atmosphere of Mars, at least 10^3–10^5 meteorites per year in excess of 10 g should impact Mars without being oxidized during delivery. These meteorites are expected to contain organics because they are shielded from the ultraviolet (UV) radiation (Bland & Smith 2000). However, energetic particles from galactic cosmic rays (GCRs) can interact with the meteoritic matter and with the Martian surface (Pavlov et al. 2012). The cosmic-ray exposure may result in the in situ synthesis of complex organic molecules such as formaldehyde (H_2CO), acetaldehyde ($HCOCH_3$), and glycolic acid ($HOCH_2COOH$) from simple precursors like carbon dioxide (CO_2) and water (H_2O) (Hubbard et al. 1971).

Once deposited on the Martian surface, the organic molecules are exposed to UV photons, cosmic rays, and oxidizing agents, which can lead to the degradation of these organics. A popular hypothesis suggests that the degradation of the organics requires solid catalysts: anatase (TiO_2, Chun et al. 1978; Pang et al. 1982), goethite (α-FeOOH), and hematite (α-Fe_2O_3) (Shkrob & Chemerisov 2009; Shkrob et al. 2011a, 2011b). It is worth noting that not only the catalytic effect of metal oxides but also the influence of phyllosilicates was studied recently (Poch et al. 2015). These silicates were found to act as photoprotective reagents. Alternative scenarios proposed an impact of interaction of plasmas within dust storms (Mills 1977; Melnik & Parrot 1998; Atreya et al. 2006) and oxidants like hydrogen peroxide (H_2O_2, Oyama & Berdahl 1977; Encrenaz et al. 2012), superoxides (O_2^-, Oyama & Berdahl 1979), and perchlorates (ClO_4^-, Ming et al. 2009; Navarro-González et al. 2010) present within the Martian soil. The presence of oxidants is the most widely accepted explanation for the lack of organics on the surface of Mars, as proposed by the Viking (Biemann et al. 1976) and Phoenix (Sutter et al. 2009) landers, and the lower-than-expected abundance of organics, as revealed by the Curiosity Rover (Freissinet et al. 2015). It should be emphasized that these oxidants are assumed to be present only in the upper few centimeters of the Martian soil because their diffusion into the soil is limited by the porosity of the rock, so organics that can be found in deeper layers are thought not to be affected (Bullock et al. 1994).

The effect of GCRs on the organics deposited on Mars is also an important topic that should be discussed. Since Mars has only a thin (and variable) atmosphere of roughly 7 mbar and has lacked a global magnetic field over the past few billion years (Acuña et al. 1998; Armstrong et al. 2004), its surface has been bombarded continuously by high-energy particles. In spite of this fact, their energy deposition on the surface chemistry is usually ignored because the total energy flux from galactic and solar cosmic rays (SCR) is four orders of magnitude lower than

that of the solar UV photons (Pavlov et al. 2012). However, UV radiation is effectively absorbed in the upper few millimeters of the Martian surface (Cockell & Raven 2004), whereas cosmic rays can penetrate up to several meters below the surface (Pavlov et al. 2012). This makes cosmic rays an excellent candidate to explain the destruction of organic compounds in the deeper Martian soil.

To estimate the actual impact of cosmic rays on organics, Pavlov et al. calculated the radiation doses from SCRs and GCRs (Pavlov et al. 2012). This study revealed that the preservation of ancient complex organic molecules in the upper 10 cm of the Martian regolith can be problematic: at 5–10 cm depths, the accumulated dosage after 1 billion years computes to about 5×10^7 Gyr, which is equivalent to an exposure of about 39 eV per glycine (H_2NCH_2COOH) molecule on the surface. Hence, ancient complex organics would have decomposed in 300 Myr. Although the calculations did not include the effect of secondary oxidation processes from ionization of the mineral matrix, in situ measurements carried out by the Radiation Assessment Detector (RAD) instrument on board the Curiosity Rover depicted a good agreement with the calculated dosages reaching the Martian surface (Hassler et al. 2014). It should be emphasized that during the calculations of Pavlov et al. only the degradation of ancient organics was examined. The continuous deposition from meteorites and interplanetary dust particles was not taken into consideration: in comparing the deposition via exogenous delivery (ten Kate et al. 2005) and the destruction caused by cosmic rays, the latter is likely offset by the former.

As a consequence, organics are still expected to be abundant enough at the ppbw level on the Martian surface or at least within the regolith subsurface of the planet that they should be detectable. Considering this conclusion, multiple in situ experiments have been carried out to find these organics on Mars. However, data from the Viking (Biemann et al. 1976; Biemann & Bada 2011) and Phoenix (Hecht et al. 2009; Sutter et al. 2009) landers excluded the presence of organic compounds, although a reanalysis of the results from these instruments concluded that they may have been overlooked (Navarro-González et al. 2010). Recently, trace amounts of dichloroalkanes ($C_nH_{2n}Cl_2 < 70$ ppbw) and chlorobenzene (C_6H_5Cl, 150–300 ppbw) were detected by the Sample Analysis at Mars instrument of the Curiosity Rover during pyrolysis experiments (Leshin et al. 2013); they possibly formed as a result of the reaction between aliphatic and aromatic organics and ClO_4^-, both originating from the Martian soil (Freissinet et al. 2015). It is worth noting that sulfate minerals may also help decompose organics during pyrolysis (Lewis et al. 2015). The presence of terrestrial carbon in the pyrolysis chamber cannot be excluded completely, but it is thought that they are indigenous to the Martian sample (Freissinet et al. 2015). Nevertheless, it seems very likely that these organics are present in the Martian subsurface in trace amounts.

To date, multiple laboratory experiments have been performed in terrestrial settings in an attempt to rationalize the results of the Mars landers by examining the destruction of the organics under simulated Martian conditions. Among them, amino acids and especially glycine as the simplest one have been the focus of interest because they represent the smallest building blocks of proteins, which are essential for life as we know it. One of the earliest studies, conducted by Oró and Holzer, found that oxygen greatly facilitates the decomposition of organics (Oró & Holzer 1979). They investigated glycine samples that were practically unchanged after broadband UV photolysis (200–300 nm). However, the amino acid concentration decreased to less than 1% of the original amount when the irradiation was carried out in the presence of a molecular oxygen (O_2) atmosphere. The authors discovered similar trends also for adenine and naphthalene. This led to the general suggestion that the combined effect of UV photolysis and the presence of oxidizing agents is crucially needed for the decomposition of organic molecules on the Martian surface.

A more recent study investigated the photodecay of glycine under more realistic Martian conditions using Mars-analog soil. This work concluded that UV photolysis alone decomposes organics faster than they accumulate on the surface (Stoker & Bullock 1997). This experiment was repeated under pure helium with similar results, suggesting that oxygen does not need to be present, contrary to the conclusions of Oró & Holzer (1979); the difference between these two measurements was whether they used Mars-analog soil or not. Decomposition of glycine was also examined along with D-alanine ($H_2NCH(CH_3)COOH$) when irradiated with Mars-like UV fluxes; modeling revealed that half-life times of these compounds are on the order of 10^7 yr when embedded in regolith, which means that they outpace the influx of meteor and interplanetary dust particles (ten Kate et al. 2005). Later, the effect of the presence of CO_2 and a low temperature relevant to Mars (210 K) on glycine decomposition was explored as well. These works revealed that while CO_2 had absolutely no effect on the decomposition kinetics, lowering the temperature decreased the decomposition rate by a factor of about seven (ten Kate et al. 2006). This work also investigated the effect of H_2O, and no evidence of H_2O affecting the destruction rates was found. Subsequently, a series of experiments focused on the photodegradation of organics including glycine on the *International Space Station* under filtered solar radiation that mimics the Martian UV radiation conditions (Cottin et al. 2012; Noblet et al. 2012; Bertrand et al. 2015). The same research group also studied the UV decomposition of glycine under simulated Martian conditions in a laboratory environment by photolyzing glycine at wavelengths between 235 and 210 nm, observing mainly CO_2 loss along with methylamine (CH_3NH_2) formation (Poch et al. 2013, 2014).

It should be pointed out that part of the previous experiments did not exploit an in situ analysis of the products formed, explored the decomposition only via UV irradiation, and were carried out at relatively high temperatures, higher than 220 K, where solid glycine may have three different zwitterionic crystalline (α-, β-, and γ-$^+H_3NCH_2COO^-$, with α being the most stable at room temperature) structures. However, at lower temperatures (below 140 K), it can also coexist in an amorphous form that can be both zwitterionic or nonzwitterionic depending on the preparation method. It should be pointed out that cosmic-ray irradiation also plays an important role in the decomposition of organics. Compared to the photolysis of Mars-analog samples and organics, only limited information exists on the destruction of these organics by GCRs under realistic Mars conditions.

The first experiment investigating the effects of GCRs was carried out just a decade ago (Kminek & Bada 2006). Gerakines et al. (2012) performed an experiment similar to the study conducted by ten Kate et al. (2005) by exploring the

Table 1
Summary of Previous Experimental Results on the Radiolysis of Glycine (H_2NCH_2COOH) under Martian Conditions

Glycine Sample	Atmosphere (mbar)	Temperature (K)	Radiation	Admixtures	Products	References
Adsorbed on quartz (SiO_2) powder	various levels of O_2	263	broadband UV (200–300 nm)	⋯	⋯	Oró & Holzer (1979)
Powder	1. 100, 95.59% CO_2, 4.21% argon (Ar), 0.11% O_2, 0.09% CO 2. pure helium (He)	293	broadband UV(>210 nm) for up to 5 weeks	palagonite	CH_4, ethane (C_2H_6), ethylene (C_2H_4), propane (C_3H_8)	Stoker & Bullock (1997)
160–400 nm thick films on silicon (Si) disk	4×10^{-6}	293	1. 120–180 nm for 2 hr 2. 190–400 nm for 40 hr	⋯	⋯	ten Kate et al. (2005)
300 ± 50 nm thick films on Si disk	1. 7, CO_2 2. 10, 50% CO_2, 50% H_2O	210	broadband UV(>190 nm) for 24 hr	⋯	⋯	ten Kate et al. (2006)
300–600 nm thick films on SiO_2 and/or magnesium fluoride (MgF_2)	⋯	288 on average	solar UV for 1190–1958 hr	⋯	⋯	Cottin et al. (2012), Noblet et al. (2012)
295 ± 19 nm thick films on magnesium fluoride (MgF_2)	6 ± 1, molecular nitrogen (N_2)	218 ± 2	broadband UV (190–400 nm)	⋯	H_2O, formic acid (HCOOH), CH_3COOH, *glycine oligopeptides* ($(–HN–CH_2–CO-)_n$)	Poch et al. (2013)
295–499 nm thick films on magnesium fluoride (MgF_2)	6 ± 1, N_2	218 ± 2	broadband UV (190–400 nm)	⋯	CO_2, CH_4, *hydrogen cyanide* (*HCN*), NH_3, $(-HN-CH_2–CO–)_n$	Poch et al. (2014)
Thin layer on magnesium fluoride (MgF_2) window	6 ± 1, N_2	218 ± 2	broadband UV (190–400 nm)	nontronite phyllosilicate		Poch et al. (2015)
Thin films on magnesium fluoride (MgF_2)	⋯	⋯	solar UV for 2843 hr	with or without meteorite powder	⋯	Bertrand et al. (2015)
Powder	⋯	⋯	γ-rays from ^{60}Co source	⋯	"volatiles"	Kminek & Bada (2006)
500–2000 nm thick films on aluminum (Al) mirror	7×10^{-7}	15, 100, 140	0.8 MeV protons (p^+)	with or without H_2O ice	CO_2, CH_3NH_2	Gerakines et al. (2012)
1000–4000 nm thick films on Al mirror	7×10^{-7}	15–300	0.8 MeV p^+	glycine : H_2O ice mixtures with different ratios	CO_2	Gerakines & Hudson (2013)
300–1600 nm thick films on zinc selenide (ZnSe) or potassium bromide (KBr)	1×10^{-8}	300	1 MeV p^+	⋯	H_2O, $(–HN–CH_2–CO–)_n$	Pilling et al. (2013)
800–4600 nm thick films on ZnSe	5×10^{-7}	14, 300	2 keV electrons (e^-)	⋯	CO_2, CO	Pilling et al. (2014)

Table 1
(Continued)

Glycine Sample	Atmosphere (mbar)	Temperature (K)	Radiation	Admixtures	Products	References
80–900 nm thick films on Si mirror	5×10^{-8}	20–300	120–200 nm UV and 2 keV e^-	1. – 2. 60 nm H_2O ice shield	UV: CO_2, CO, carbon oxides (C_xO_y), CH_3NH_2 e^-: CO_2, CO, and cyanate (OCN^-)	Maté et al. (2014)
90 ± 10 nm thick films on Si mirror	2×10^{-8}	20, 40, 90, 300	2 keV e^-	1. – 2. 150 nm H_2O ice shield	CO_2, CO, OCN^-, cyanide (CN^-), (*–HN–CH_2–CO–*)$_n$	Maté et al. (2015)
3000 nm thick films on Al mirror	7×10^{-7}	25, 50, 75	0.8 MeV p^+	glycine : CO_2 ice mixtures with different ratios	CO_2	Gerakines & Hudson (2015)

Note. The table consists of two parts: the first one summarizes the UV and the second one pays attention to the GCR-analog experiments, and both of them are in chronological order. Italics: tentative identification.

radiolytic destruction of different amino acids (glycine, alanine, and phenylalanine [$C_6H_5CH_2CH(NH_2)COOH$], respectively) at low temperatures (15, 100, and 140 K) by exposing the samples to 0.8 MeV protons to simulate cosmic rays. This study also estimated the half-lives of amorphous zwitterionic glycine for Martian environments and found them to be similar ($\approx 10^8$ yr) to values determined previously by ten Kate et al. (2005). It is interesting to note that even different crystalline forms are not equally sensitive to irradiation: based on the results of Pilling et al. (Pilling et al. 2013), β-glycine is more stable than the α form. Here the half-life of the former was determined to be five times longer than that of the latter when irradiated with 1 MeV protons. In a recent paper, the radiation stability of nonzwitterionic glycine diluted in CO_2 ices (CO_2-to-glycine ratios varied between 75:1 and 380:1) was examined, and it was shown that it is less resistant to irradiation in dry ice than it is in H_2O ice (Gerakines & Hudson 2015) and destruction in H_2O ice decreases by 75% when increasing the temperature from 15 to 140 K (Gerakines & Hudson 2013).

Besides energetic protons, electrons were also exploited to irradiate Mars-analog organics, which simulate the secondary electrons formed in the track of GCRs once they have penetrated solid matter like Martian surface minerals and organics (Bennett et al. 2005; Bennett & Kaiser 2007). The decay of glycine was studied upon 2 keV electron irradiation, which led to a gradual disappearance of glycine along with a formation of CO_2; surprisingly, no other species, like the other decarboxylation product CH_3NH_2 or deamination products ammonia (NH_3) and acetic acid (CH_3COOH), could be identified (Maté et al. 2014). The few hundred nanometer thick layer of amino acid could not be destroyed; the 60 nm H_2O ice layer deposited on top of the amino acids provided a partial shielding from the energetic electrons. Another recent paper investigated the stability of a thin glycine film (90 nm) toward exposure to 2 keV electrons (Maté et al. 2015). Destruction cross sections, which are proportional to the rate of destruction, radiolysis yields, and half-lives for samples were reported for 20, 40, 90, and 300 K. Interestingly, the authors concluded that the rate of destruction is invariant of the temperature; further, the decay rate of β-glycine was found to be larger by a factor of two at 300 K compared to the low temperatures, at which the zwitterionic amorphous form prevails. Besides, the calculated half-life times of the amorphous form were similar to the data from experiments carried out with megaelectronvolt protons (Gerakines et al. 2012). It is worth noting that these findings contradict the results from Pilling et al. (2014). According to their results, the dissociation cross section of crystalline glycine is inversely proportional to the temperature; that is, glycine decomposes five times faster at 14 K than at 300 K. Furthermore, half-life times of the α and β forms were found to be at least an order of magnitude longer than the half-life times determined by competing groups.

Despite extensive research on the destruction of amino acids on Mars as compiled in Table 1, not a single experimental study has probed the effects of ClO_4^- on the radiolysis of organics. They occur throughout the solar system (Jackson et al. 2015) and are thought to be significant oxidants in the soil of Mars with abundances as high as 0.5%–1.0% by weight (Davila et al. 2013), as detected by the Phoenix lander (Hecht et al. 2009) and the Curiosity Rover (Leshin et al. 2013). Their atmospheric origin via gas-phase oxidation appears unlikely; instead, formation may rely on heterogeneous photocatalytic or radiation-induced surface reactions and via direct meteoritic delivery (Kim et al. 2013; Smith et al. 2014; Carrier & Kounaves 2015). Note that ClO_4^- is most likely in its hydrated form with magnesium (Mg^{2+}) or calcium (Ca^{2+}) as counter-cations. These findings were also confirmed via laboratory experiments (Chevrier et al. 2009; Kounaves et al. 2014; Nuding et al. 2014) and theoretical calculations (Marion et al. 2010; Toner et al. 2014) revealing that hydrated ClO_4^- compounds such as magnesium perchlorate hexahydrate ($Mg(ClO_4)_2 \cdot 6H_2O$) are stable under Martian conditions.

Since ClO_4^- and its hydrated compounds are suggested to be responsible for the destruction of organics on Mars in the presence of GCRs (Encrenaz et al. 2012), the effect of GCRs on the decomposition of organics under realistic Mars temperatures from 160 to 260 K (Nuding et al. 2014) has yet to be evaluated. The goal of the present investigation is to explore *quantitatively* the *decay kinetics* and the *degradation products* of pure glycine and of glycine in the presence of perchlorates—namely, $Mg(ClO_4)_2 \cdot 6H_2O$—at Mars-relevant temperatures from 160 to 210 K. We also aim to unravel the reaction products formed in these processes online and in situ to gain a hitherto-lacking understanding of the reaction pathway(s) on the ClO_4^--assisted decomposition of glycine on the Martian surface. Monitoring the electron radiolysis of Mars-relevant samples online and in situ in a state-of-the-art simulation chamber at ultra-high-vacuum (UHV) conditions helps us understand the chemical fate of organic materials and answers the long-standing question, why can organics only be found in trace amounts on the surface and subsurface of Mars? These transformative concepts on the decomposition mechanisms of the organics will help us to develop new ideas on how complex organic molecules may have been preserved throughout the (early) solar system.

2. EXPERIMENTAL

The experiments were conducted in a contamination-free UHV stainless steel chamber evacuated to a few $\times 10^{-10}$ torr by exploiting oil-free turbomolecular pumps and dry scroll backing pumps (Bennett et al. 2004). A polished silver mirror located in the center of the chamber serves as a substrate and is mounted onto a rotatable cold finger attached to a two-stage, closed-cycle helium refrigerator (CTI-Cryogenics Cryodyne 1020, compressor: CTI-Cryogenics 9600). The mirror and the cold finger are sandwiched with indium foil to maximize the thermal conductivity. In the separate experiments, the substrate was cooled down to 10, 160, 210, and 260 K with an accuracy of ± 0.3 K.

Pure glycine (H_2NCH_2COOH, Fluka, 99.0+%) and magnesium perchlorate hexahydrate ($Mg(ClO_4)_2 \cdot 6H_2O$, Sigma Aldrich, 99.0+%) were used to prepare samples approximately 500 nm thick. The samples were made by dissolving 0.072 g glycine for pure glycine films or 0.070 g $Mg(ClO_4)_2 \cdot 6H_2O$ with 0.016 g glycine for the glycine–$Mg(ClO_4)_2 \cdot 6H_2O$ mixtures in a molar ratio of 1:1 in 50 ml distilled H_2O, adding 0.5 ml of the solutions on the surface of the silver substrate and evaporating the solvent H_2O completely at 323 to 333 K, and finally the newly made samples were put into the vacuum chamber. Care has to be taken that the solution covers the complete surface of the silver wafer to obtain a sample with an even thickness. The average thicknesses can then be calculated from the sample masses by knowing the silver substrate area

Table 2
Summary of CASINO Simulations on the Electron Radiolysis Experiments of Glycine and Glycine–$Mg(ClO_4)_2 \cdot 6H_2O$

Parameter	Glycine	Glycine–$Mg(ClO_4)_2 \cdot 6H_2O$
Irradiated area (cm^2)	3.2 ± 0.3	3.2 ± 0.3
Angle of incidence (°)	75	75
Irradiation time (s)	3600 ± 2	3600 ± 2
Applied electron current (nA)	100.0 ± 10	100.0 ± 10
Average density of film (g cm^{-3})	1.61 ± 0.01	1.80 ± 0.19
Molar masses of molecules in film (g mol^{-1})	75.06	75.06 (glycine), 331.30 ($Mg(ClO_4)_2 \cdot 6H_2O$)
Initial energy of the electrons (keV)	5.00	5.00
Average backscattered energy of the electrons (keV)	2.81 ± 1.12	2.88 ± 1.15
Average transmitted energy of the electrons (keV)	0.00 ± 0.00	0.00 ± 0.00
Simulated average penetration depth (nm)	277 ± 55	253 ± 51
Fraction of backscattered electrons (%)	7.12 ± 1.42	10.4 ± 2.1
Fraction of transmitted electrons (%)	0.00 ± 0.00	0.00 ± 0.00
Dose per molecule (eV)	9.4 ± 0.2	10.1 ± 0.3 (glycine), 36.2 ± 1.0 ($Mg(ClO_4)_2 \cdot 6H_2O$)

Note. The error values were determined emipirically (irradiated area, irradiation time, applied electron current), taken from the literature (glycine and $Mg(ClO_4)_2 \cdot 6H_2O$ densities), or estimated by the CASINO simulations.

(9.0 cm^2) and the density of the sample films of 1.61 ± 0.01 g cm^{-3} (Houck 1930; the uncertainty was estimated based on the density values listed therein) for the pure glycine and the average density of 1.80 ± 0.19 g cm^{-3} for the pure glycine and the glycine–$Mg(ClO_4)_2 \cdot 6H_2O$ 1:1 mixture, respectively. The average mixture density value was evaluated by assuming that it is equal to the arithmetic mean of the density of the components weighted by their molar fractions (Luna et al. 2012), namely, that of the glycine (1.61 ± 0.01 g cm^{-3}) and the $Mg(ClO_4)_2 \cdot 6H_2O$ (1.98 ± 0.03 g cm^{-3}; Lewis 2007; because its uncertainty was unavailable, it was determined empirically using the pycnometric method). The determined average thicknesses are 480 ± 60 nm and 530 ± 60 nm for pure glycine and the glycine–Mg $(ClO_4)_2 \cdot 6H_2O$ mixture, respectively, based on the substrate area, the sample masses (0.0007 ± 0.0001 g for pure glycine and 0.0009 ± 0.0001 for glycine and for the glycine–Mg $(ClO_4)_2 \cdot 6H_2O$ mixture), and the densities.

Each sample was then irradiated with energetic electrons (5 keV) for 60 minutes at a current of 0 nA (blank experiment) and 100 ± 10 nA generated by a SPECS EQ 22/35 electron gun measured by a Faraday cup mounted between the electron gun and the sample before and after irradiation, which leads to an exposure of the samples by (7.0 ± 0.7) × 10^{14} electrons cm^{-2} over 3.2 ± 0.3 cm^2. After the irradiation, the samples were kept at the temperature of irradiation for 60 minutes and were then heated to 300 K at 0.5 K $minute^{-1}$. During the irradiation and in the warm-up phase, the chemical modifications of the samples were probed online and in situ using a Fourier transform infrared spectrometer (FTIR; Thermo Nicolet 6700) and a quadrupole mass spectrometer (QMS; Pfeiffer Vacuum QMG 422). The FTIR spectrometer collected 196 scans of the samples for 2 minutes from 4000 to 400 cm^{-1} at a resolution of 4 cm^{-1}, while the QMS operated in the residual gas analyzer mode with an electron impact ionization energy of 90 eV and an emission current of 0.7 mA to detect the subliming species.

The average dose per molecule deposited was computed via Monte Carlo simulations, taking the scattering coefficients and the energy deposited from the electrons into consideration (Table 2). For this, the CASINO (v2.42) software (Drouin et al. 2007) was utilized by simulating the exposure of pure glycine and the glycine–$Mg(ClO_4)_2 \cdot 6H_2O$ 1:1 mixture, with a thickness of 500 nm and a density of 1.61 ± 0.01 g cm^{-3} for glycine and 1.80 ± 0.19 g cm^{-3} for the mixture. A total of 10^6 trajectories were simulated to mimic the energy-transfer processes. These calculations yield average doses of 9.4 ± 0.2 eV and 10.1 ± 0.3 eV per glycine molecule in pure glycine and in the glycine–$Mg(ClO_4)_2 \cdot 6H_2O$ 1:1 mixtures. These dosages, based on the results of Pavlov et al. (2012, see Introduction), correspond to what a glycine molecule receives in 240 My at a depth of 5–10 cm. Average penetration depths of 277 ± 55 nm and 253 ± 51 nm, respectively, were computed. Note that the average penetration depth is lower than the thickness of the samples (480 ± 60 nm and 530 ± 60 nm, respectively). Therefore, the impinging electrons only interact with the sample but not with the silver substrate.

3. RESULTS

3.1. Infrared Spectrum of Glycine

The infrared (IR) spectra of crystalline and amorphous glycine are well known, and the ones obtained at four different temperatures (260, 210, 160, 10 K) during our experiments correlate exceptionally well with the results of previous experimental (Maté et al. 2011; Gerakines et al. 2012; Rosado et al. 1998) and theoretical works (Chowdhry et al. 2008; Kayi et al. 2011, 2012), particularly with the IR spectrum of the

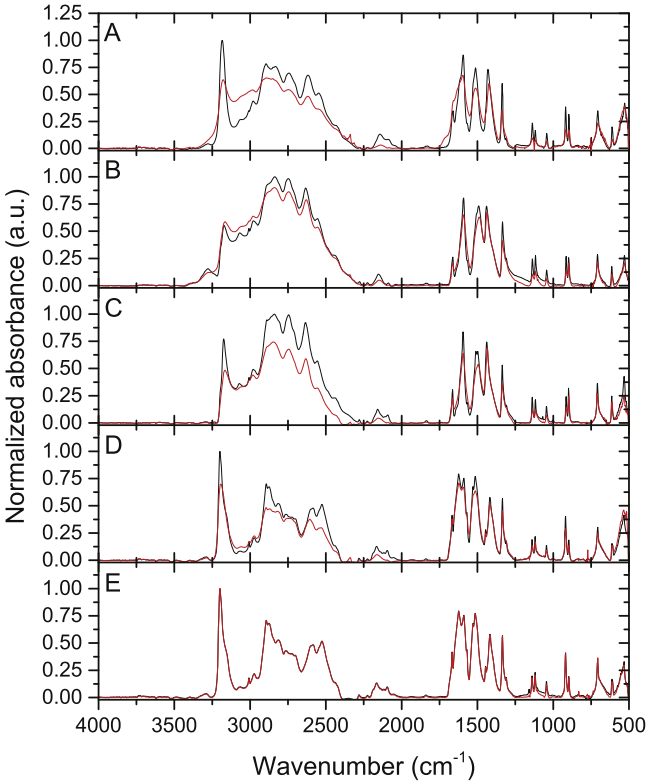

Figure 1. Infrared spectra of glycine before (black line) and after irradiation (red line) at 260 K (A), 210 K (B), 160 K (C), and 10 K (D) along with the 10 K blank experiment (without irradiation, E).

crystalline zwitterionic form. Infrared spectra taken over the range of 4000–400 cm^{-1} prior to and after the irradiation are shown in Figure 1, while assignments of the absorption peaks are compiled in Table 3. An extremely broad and intense band is detected in the 3250–2400 cm^{-1} region, consisting of the vibrations associated with the alkylammonium (ν_{as} NH_3^+, antisymmetric stretching, 3180 and 3075 cm^{-1}) and methylene (ν_{as} CH_2 and ν_s CH_2, antisymmetric and symmetric stretching modes at 3007 and 2980 cm^{-1}, respectively) groups. The broadening is considered to be caused by Fermi resonance of the alkylammonium symmetric stretching (ν_s NH_3^+) and combination vibrations, involving predominantly the bending vibrations (Table 3; Rosado et al. 1998). Another wide but structured feature can be found between 1700 and 1250 cm^{-1}, resulting from the overlapping of the antisymmetric (1670 and 1640 cm^{-1}) and symmetric (1530 and 1490 cm^{-1}) bending modes of ammonium (δ_{as} NH_3^+ and δ_s NH_3^+), the bending mode of methylene (δ CH_2, at 1445 cm^{-1}), the antisymmetric and symmetric stretching of the carboxylic (ν_{as} COO^- and ν_s COO^-, 1590 and 1430 cm^{-1}) group, and the wagging and twisting of the methylene groups (ω CH_2 and tw CH_2, 1335 and 1310 cm^{-1}, respectively) of the zwitterionic glycine molecule.

Absorption features with lower intensities can be identified in the regions of 2400–1700 cm^{-1} and 1250–400 cm^{-1}, with combinational bands (e.g., the combination of the antisymmetric bending of ammonium and the torsion of C–N, δ_{as} NH_3^+ + τ CN, at 2140 cm^{-1}) in the former. The latter part of the spectrum comprises the rocking vibration of ammonium (ρ NH_3^+, at 1140 and 1120 cm^{-1}) and methylene (ρ CH_2, at around 915 cm^{-1}), the C–N and C–C stretching modes (ν CN and ν CC, 1045 and 895 cm^{-1}, respectively), the bending of a carboxylic anion (δ COO^-, 710 cm^{-1}), and that of the C–C–O chain (δ CCO^-, 530 cm^{-1}) in the zwitterionic glycine molecule. The wagging mode of the carboxylic anion (ω COO^-, 610 cm^{-1}) and probably the C–N torsional vibration (τ CN, 485 cm^{-1}; note that intermolecular interactions can greatly affect the frequency of this vibrational mode; Rosado et al. 1998) are also included in this region.

Alterations in the IR spectra of the pure glycine samples can be induced when irradiated with high-energy electrons during the experiments. This can be verified when comparing the irradiated sample spectra (Figure 1(D)) to the pristine sample (Figure 1(E)) measured at 10 K: keeping the sample at this temperature for 1 hr does not alter its IR spectrum at all, whereas irradiating the sample for the same time causes significant changes in it, which is in complete agreement with the results of previous experimental works (Pilling et al. 2014; Maté et al. 2014, 2015). In general, all features decrease and broaden upon irradiation; the simultaneous degradation, amorphization, and oligomerization (to oligopeptides, $(–HN–CH_2–CO–)_n$; Kaiser et al. 2013; Pilling et al. 2013) of the crystalline organic sample may account for this phenomenon. Note that while the peak intensities decrease, they also merge as a consequence of widening, resulting in even broader bands; this is especially valid for the experiments performed at higher temperatures as the destruction rates are expected to be higher (Section 4.1). The best examples for this broadening are the bands between 3250–2400 cm^{-1} and 1700–1250 cm^{-1} occurring principally at 260 K (Figure 1(A)). Apart from the ubiquitous decrease of absorption peaks, only one new intense emerging signal can be detected in all experiments at 2340 cm^{-1}, which belongs to the stretching vibration of CO_2 (ν_{as} CO_2), a common decarboxylation product of amino acids when irradiated, as identified by numerous works previously as well (Gerakines et al. 2012; Gerakines & Hudson 2013; Pilling et al. 2014; Maté et al. 2014, 2015). However, there is significant evidence of other irradiation products in the spectra that can be responsible for the widening of the peaks (Section 4.2).

Apart from fact that the absorption features change upon electron irradiation, the frequencies and peak intensities of all the listed vibrations have a temperature dependence. The prime example of this behavior is the band containing the antisymmetric bending of ammonium (δ_{as} NH_3^+) and the antisymmetric stretching of the carboxylic (ν_{as} COO^-) group: at 10 K they can be detected as two distinguishable (although partially overlapping) signals at 1623 and 1590 cm^{-1}. However, at higher temperatures, the intensity of the higher-frequency signal decreases and can be observed as a shoulder only. Also, the feature containing the bending mode of methylene (δ CH_2, at 1445 cm^{-1}) and the symmetric stretching of the carboxylic (ν_s COO^-, 1430 cm^{-1}) groups can be seen as one broad peak at higher temperatures; it splits into a doublet at 10 K (Figure 1(D)). In the higher-frequency regions of the IR spectra, the antisymmetric stretching vibrational signals of ammonium (ν_{as} NH_3^+, 3180 and 3075 cm^{-1}) merge, leading to one broad band at higher temperatures; however, one can easily observe the change in frequencies and their intensity ratios of Fermi resonances and combinational bands when altering the experimental temperature. The signal of the CO_2 antisymmetric stretching vibration (ν_{as} CO_2, 2340 cm^{-1}), whose peak emerges upon irradiation, also depends on the temperature: its integrated area is growing faster at higher temperatures, indicating higher

Table 3
Infrared Absorptions for Pure Glycine and Irradiation-induced Changes

Assignment[a,b]	160 K				10 K			
	Band Position (cm^{-1})[c]				Band Position (cm^{-1})[c]			
	Before Irrad.	After Irrad.	Signal Strength[d]	Change upon Irrad.[e]	Before Irrad.	After Irrad.	Signal Strength[d]	Change upon Irrad.[e]
δ_{as} $NH_3^+ \times 2$[f], ν_{as} $COO^- \times 2$[f], δ_s $NH_3^+ \times 2$[f]	3276.2	3276.2	w	b(+)	3320.6sh, 3297.6sh, 3280.5, 3238.5sh	3320.6sh, 3297.6sh, 3280.5	m, b	⋯
ν_{as} NH_3^+	3187.3, 3069.2w	3177.9	s	−, b(+)	3195.6sh, 3174.8, 3069.5w	3197.9sh, 3167.0	s	−, b(+)
ν_{as} CH_2	3009.8	3005.9	w	⋯	3008.3	3007.6	w	−, b
ν_s CH_2	2979.2	2983.7	w	⋯	2976.8, 2962.1sh	2980.7	w	−, b
ν_s NH_3^+[g]	2894.4, 2830.0	2894.4, 2830.0	s, b	−, b(+)	2889.5sh, 2836.7, 2802.6sh	2889.5sh, 2836.7, 2802.6sh	s, b	−, b(+)
ν_s NH_3^+[g]	2743.2, 2701.4sh	2743.2, 2701.4sh	s, b	−, b	2762.2sh, 2745.8, 2710.1sh	2762.2sh, 2745.8, 2710.1sh	s, b	−, b
ν_s NH_3^+[g]	2617.8	2617.8	s, b	−, b	2635.6, 2613.3sh	2635.6, 2613.3sh	s, b	−, b
ν_s NH_3^+[g]	2547.5	2547.5	s, b	−, b	2554.5, 2532.3	2555.8, 2531.9	m, b	−, b
ν_s NH_3^+[g]	2433.2	2433.2	sh	⋯	2440.8	2440.8	sh	⋯
ν_{as} CO_2[h]	⋯	2338.8	w	+	⋯	2338.7	w	+
ν_{as} $COO^- + \omega$ COO^-[i]	2225.7	⋯	w	⋯	2278.0, 2225.6	⋯	w	⋯
δ_{as} $NH_3^+ + \tau$ CN[i]	2143.8, 2086.4	2138.1, 2086.4	w, b	⋯	2154.9, 2087.3	2149.2	w, b	−, b
δ_s $NH_3^+ + \delta$ NCC[i]	1828.9	⋯	vw	⋯	1837.7	1837.7	vw	⋯
δ_{as} NH_3^+	1662	1703.6sh, 1662	m	−, b(+)	1673.9sh, 1662.9	1677.9sh, 1664.9	m	−, b(+)
δ_{as} NH_3^+	1634.6, 1619.7	1634.6, 1619.7	sh	−, b(+)	1639.4, 1609.3	⋯	sh	−, b(+)
ν_{as} COO^-	1593.2, 1565.5	1593.2, 1565.5sh	s	−, b(+)	1591.7, 1562.3sh	1591.7	s	−, b(+)
δ_s NH_3^+	1525.6sh, 1512.5, 1497.8sh	1525.6sh, 1512.5, 1497.8sh	s	−, b(+)	1521.5sh, 1506.1sh, 1493.8	1506.3sh, 1488.4	s	−, b(+)
δ CH_2, ν_s COO^-	1446.1sh 1433.0, 1396.7sh	1446.1sh, 1424.1	s	−, b(+)	1446.3sh, 1439.6 1404.5sh	1446.3sh, 1436.3	s	−, b(+)
ω CH_2	1336.8	1336.8	m	−, b(+)	1334.5, 1322.5sh	1335.2	m	−, b(+)
tw CH_2	1309.9	1309.9sh	w	−, b(+)	1309.0	1309.0	sh	−, b
ρ NH_3^+	1137.9	1137.9	m	⋯	1137.6	1137.6	m, b	⋯
ρ NH_3^+	1118.3	1118.3	m	⋯	1117.1	1117.1	m	−, b
ν CN	1043.5	1043.5	m	⋯	1043.1	1043.1	m	−, b

Table 3
(Continued)

Assignment[a,b]	160 K				10 K			
	Band Position (cm^{-1})[c]		Signal Strength[d]	Change upon Irrad.[e]	Band Position (cm^{-1})[c]		Signal Strength[d]	Change upon Irrad.[e]
	Before Irrad.	After Irrad.			Before Irrad.	After Irrad.		
ρ CH_2	918.0	918.0	m	−, b(+)	914.7	914.7	m	−, b(+)
ν CC	896.8	896.8	m	−, b(+)	897.8	897.8	m	−, b(+)
δ COO^-	705.7	705.7	m, b	−, b	707.5	707.5	m	−, b
ω COO^-	611.6	611.6	m	−, b	613.6	613.6	m	−, b
δ CCO^-	528.8	528.8	m	−, b	530.3	530.3	m, b	−, b(+)
τ CN	485.6	⋯	w	⋯	487.2	484.5	w	−, b(+)
δ_{as} $NH_3^+ \times 2$[f] ν_{as} $COO^- \times 2$[f] δ_s $NH_3^+ \times 2$[f]	3322.4sh, 3301.2, 3286.2, 3234.9sh	3322.4sh, 3301.2, 3286.2	vw, b	⋯	3323.8sh, 3305.9sh, 3289.6	3323.8sh, 3305.9sh 3286.7	w, b	−, b(+)
ν_{as} NH_3^+	3197.9sh, 3175.9, 3073.6w	3197.9sh, 3175.9	s	−, b(+)	3201.1, 3153.0sh, 3075.9	3193.3, 3174.3sh, 3059.6	s, b	b(+)
ν_{as} CH_2	3007.9	3007.9	w	−, b	3008.4	3006.5	w	b
ν_s CH_2	2981.2, 2968.2sh	2981.2	w	−, b	2973.8	2972.1	w	b
ν_s NH_3^+[g]	2891.1sh, 2837.0, 2803.8sh	2891.1sh, 2837.0, 2803.8sh	s, b	−, b	2892.9, 2875.9, 2846.0sh	2893.9	s, b	−, b(+)
ν_s NH_3^+[g]	⋯	⋯	⋯	⋯	2813.8	2819.2	m	⋯
ν_s NH_3^+[g]	2765.1sh, 2746.0, 2711.1sh	2765.1sh, 2746.0, 2711.1sh	s, b	−, b	2764.2, 2718.9, 2696.1	2733.9, 2696.1	w, b	⋯
ν_s NH_3^+[g]	2635.5, 2612.3sh	2635.5, 2612.3sh	s, b	−, b	2603.3sh, 2579.6	2603.3sh, 2579.6	s	−, b
ν_s NH_3^+[g]	2555.8, 2531.9	2555.8, 2531.9	m, b	−, b	2546.7sh, 2525.1, 2481.0sh	2546.7sh, 2525.1, 2481.0sh	s	−, b
ν_s NH_3^+	2434.1	⋯	sh	⋯	2438.8, 2423.2	2438.8, 2423.2	sh	⋯
ν_{as} CO_2[h]	⋯	2338.3	w	+	⋯	2339.4	w, b	+
ν_{as} $COO^- + \omega$ COO^-[i]	2279.0, 2226.2	⋯	w	⋯	2281.1, 2225.9	2277.8	w	−, b
δ_{as} $NH_3^+ + \tau$ CN[i]	2180.7sh, 2158.8, 2091.8	2158.8, 2091.8	w, b	−, b	2189sh, 2165.8, 2117.7, 2095.3, 2051.8	2189sh, 2162.6, 2095.3	m	−, b
δ_s $NH_3^+ + \delta$ NCC[i]	1836.7	1836.7	vw	⋯	1840.0	1840.0	vw, b	⋯
δ_{as} NH_3^+	1677.9sh, 1664.9	1677.9sh, 1664.9	m	−, b(+)	1684.8sh, 1667.5	1667.9	m	−, b(+)
δ_{as} NH_3^+	1641.6, 1612.6	1641.6, 1612.6	sh	−, b(+)	1643.9sh, 1624.4, 1616.7sh	1643.9sh, 1622.8, 1616.7sh	s	−, b(+)

Table 3
(Continued)

Assignment[a,b]	160 K				10 K			
	Band Position (cm^{-1})[c]				Band Position (cm^{-1})[c]			
	Before Irrad.	After Irrad.	Signal Strength[d]	Change upon Irrad.[e]	Before Irrad.	After Irrad.	Signal Strength[d]	Change upon Irrad.[e]
ν_{as} COO^-	1594.8, 1566.8sh	1594.8, 1566.8sh	s	−, b(+)	1588.8, 1581.8sh, 1570.5	1592.5, 1581.8sh, 1570.5	s	−, b(+)
δ_s NH_3^+	1523.5, 1511.5, 1498.2	1523.5, 1511.5, 1488.7	s	−, b(+)	1544.7sh, 1538.8sh, 1529.4	1544.7sh, 1538.8sh, 1529.4	m	−, b(+)
δ_s NH_3^+	…	…	…	…	1514.5, 1501.2sh	1514.5, 1501.2sh	s	−, b(+)
δ CH_2;	1445.7sh 1440.7, 1400.8sh	1445.7sh 1434.9, 1400.8sh	s	−, b(+)	1446.8;	1446.8;	w;	−, b;
ν_s COO^-[j]					1417.5, 1400.8sh, 1383.4sh	1417.5, 1400.8sh, 1383.4sh	s	−, b(+)
ω CH_2	1336.7, 1324.2sh	1336.7, 1324.2sh	m	−, b(+)	1335.8, 1324.0sh	1335.8, 1324.0sh	s	−, b(+)
tw CH_2	1308.5	1308.5	sh	−, b	1309.4	1309.4	w	…
ρ NH_3^+	1138.0, 1132.6sh	1138.0, 1132.6sh	m	−, b(+)	1140.4	1139.7	m	−, b(+)
ρ NH_3^+	1117.5, 1104.5sh	1117.5, 1104.5sh	m	−, b	1119.6, 1104.9sh, 1094.5sh	1119.6	m	−, b(+)
ν CN	1044.7	1044.7	m	−, b	1044.5	1044.5	m	−, b(+)
ρ CH_2	915.4	915.4	m	−, b(+)	939.2sh, 918.1	918.1	m	−, b(+)
ν CC	898.5	898.5	m	−, b(+)	896.8	896.8	m	−, b(+)
δ COO^-	708.0	708.0	m	−, b(+)	710.0, 706.2	710.0, 706.2	m	−, b(+)
ω COO^-	613.9	613.9	m	−, b(+)	611.9, 608.7sh	611.9, 608.7sh	m	−, b(+)
δ CCO^-	532.3	532.3	m, b	−, b(+)	535.4	535.0	w	b(+)
τ CN?	487.5	…	w	…	482.0	482.0	w	–

Notes.
[a] Assignments based on previous experimental studies (Rosado et al. 1998; Maté et al. 2011; Gerakines et al. 2012).
[b] ν: stretching, δ: bending, ω: wagging, tw: twisting, ρ: rocking, s: symmetric, as: antisymmetric vibrations, ?: uncertain.
[c] …: no signal, sh: shoulder, w: weak band.
[d] s: strong, m: medium, (v)w: (very) weak, sh (shoulder), (v)b: (very) broad band.
[e] …: band decreases, +: band increases, 0: no change, b: broadening, b(+): broadening with possible new bands upon irradiation.
[f] Overtone, tentative assignment.
[g] Fermi resonance; for tentative assignment see Rosado et al. (1998).
[h] Stretching vibration of irradiation product CO_2.
[i] Combinational band, tentative assignment, $\nu(\delta NCC) = 358\ cm^{-1}$ (Furić et al. 1992).
[j] The two vibrational modes can be distinguished at 10 K.

rates of formation (Section 4.1). Smaller differences between intensity ratios and frequencies can also be caused by small variances in the thickness and unevenness of the sample.

3.2. Infrared Spectrum of Glycine–Magnesium Perchlorate Hexahydrate

The IR spectra in the range 4000–400 cm^{-1} before and after the irradiation can be seen in Figure 2, and assignments of the most important bands are summarized in Table 4. By comparing the spectrum taken of glycine–$Mg(ClO_4)_2 \cdot 6H_2O$ to the one of pure glycine and to the $Mg(ClO_4)_2 \cdot 6H_2O$ spectrum (Figure 2(F)), we can visualize key spectral differences. These include the lack of the characteristic broad band between 3250 and 2400 cm^{-1} caused by Fermi resonances; instead, one (or two, depending on the experimental temperature) new absorption band is shifted toward larger wavenumbers approximately between 3500 and 2250 cm^{-1}. Shifts in band positions can also be noticed in other spectral intervals as well: good examples of that are the ammonium vibrations (δ_{as} NH_3^+ and δ_s NH_3^+) of glycine, whose maxima move by +50 and −35 cm^{-1} in the glycine–$Mg(ClO_4)_2 \cdot 6H_2O$ mixture samples compared to pure glycine. The shift of the former can be at least partly explained by the presence of crystalline H_2O, whose bending vibration can be detected in this IR region (at 1624 cm^{-1}). Other peaks belonging to glycine tend to shift only by a little (5–10 cm^{-1} at maximum, barely larger than the 4 cm^{-1} resolution of the FTIR measurement). Another new feature is the broad band between 1250 and 800 cm^{-1}, which can be assigned to the absorption of $Mg(ClO_4)_2 \cdot 6H_2O$.

The broad band(s) in the 3250–2400 cm^{-1} region consist(s) of the signals of the antisymmetric stretching vibration of ammonium (ν_{as} NH_3^+, 3245 and 3170 cm^{-1}) and methylene (ν_{as} CH_2 and ν_s CH_2, antisymmetric and symmetric stretching modes at 2985 cm^{-1}) groups, plus the symmetric and antisymmetric stretching absorption peaks of crystalline H_2O in $Mg(ClO_4)_2 \cdot 6H_2O$ (ν_s H_2O and ν_{as} H_2O, at 3555 and 3485 cm^{-1}). Similar to the case of pure glycine, the broadening of this band can likely be caused by the symmetric stretching vibration of ammonium (ν_s NH_3^+); similar to the case of pure glycine, however, this broadening results in a featureless band, and no peaks belonging to this vibrational mode can be resolved. The structured feature at 1645 cm^{-1} is a consequence of the overlapping of the ammonium antisymmetric bending mode (δ_{as} NH_3^+), the bending vibrations of the crystalline H_2O (δH_2O) in $Mg(ClO_4)_2 \cdot 6$ H_2O, and the antisymmetric stretching of the carboxylic (ν_{as} COO^-) group (Table 4). The symmetric bending mode of ammonium (δ_s NH_3^+, 1480 cm^{-1}) is shifted toward smaller frequencies by 35 cm^{-1}, while the bending mode of the methylene (δ CH_2) group merges with the symmetric stretching vibration of the carboxylic group (ν_s COO^-, 1425 cm^{-1}). This band (at 1425 cm^{-1}) and the wagging and twisting of methylene groups (ω CH_2 and *tw* CH_2, 1335 and 1315 cm^{-1}) do not show any shift compared to a pure glycine spectrum. At lower wavenumbers, the most significant band can be assigned to the absorption of $Mg(ClO_4)_2 \cdot 6H_2O$; the symmetric and antisymmetric stretching vibrations of the ClO_4^- (ν_s ClO_4^-, ν_{as} ClO_4^-) accounts for the broad peak between 1250 and 750 cm^{-1}, and this is in accordance with the findings of previous works (Miller & Wilkins 1952; Bishop et al. 2014; Hanley et al. 2015). This band has a fine structure as a consequence of the superposition with the absorption of glycine in this spectral region: the rocking vibration of ammonium (ρ NH_3^+, at 1140 cm^{-1}), the same vibrational mode of methylene (ρ CH_2) merged with the C–C stretching mode (ν CC, at around 900 cm^{-1}), and the C–N stretching mode (ν CN, 1040 cm^{-1}). The bending of the carboxylic anion (δ COO^-, 695 cm^{-1}), its wagging mode (ω COO^-, 615 cm^{-1}), and the C–C–O chain bending (δ CCO^-, 540 cm^{-1}) can be detected in a lower-frequency region of the spectra.

As was the case for glycine, irradiation with energetic electrons also changes the IR spectra of glycine–Mg $(ClO_4)_2 \cdot 6H_2O$ mixtures, which can be proven by comparing the irradiated spectrum (Figure 2(D)) taken at 10 K to the blank one (Figure 2(E)). As in the experiments carried out with pure glycine, all bands decrease and broaden upon irradiation as the simultaneous degradation, amorphization, and oligomerization (to oligopeptides, $(–HN–CH_2–CO–)_n$; Kaiser et al. 2013; Pilling et al. 2013) of the crystalline sample progress with time. Along with the reducing peak intensities, the bands tend to become broader, as is the case with the band at 3200 cm^{-1}, consisting mainly of the antisymmetric stretching vibration of ammonium (ν_{as} NH_3^+, roughly at 3245 and 3170 cm^{-1}) and the symmetric and antisymmetric absorption peaks of crystalline H_2O in $Mg(ClO_4)_2 \cdot 6H_2O$ (ν_s H_2O and ν_{as} H_2O, at 3555 and 3485 cm^{-1}), which is the best instance of this phenomenon.

Aside from the ubiquitous decrease of absorption peaks, a new emerging signal can be detected at 2340 cm^{-1}. As could also be deduced from the experiments with pure glycine, this belongs to the antisymmetric stretching vibration of the common amino acid decarboxylation product of the CO_2 (ν_{as} CO_2) molecule (Gerakines et al. 2012; Gerakines & Hudson 2013; Pilling et al. 2014; Maté et al. 2014, 2015). The formation of small amounts of carbon monoxide (CO) can also be observed upon irradiation at 10 K; its signal lies at 2131 cm^{-1}, which can be assigned to its stretching vibration (ν CO). It is very likely that there are other irradiation products in the spectra that may be at least partially the source of the broadening of the peaks (Section 4.2). Whether the samples are irradiated or not, frequencies and band intensities of the glycine–Mg $(ClO_4)_2 \cdot 6H_2O$ mixture also change when a different experimental temperature is applied. In general, the IR spectra collected at 10 K deviate the most from the data taken at higher temperatures. For instance, the band of the ammonium antisymmetric stretching vibration (ν_{as} NH_3^+) shifts to higher wavenumbers and overlaps with the stretching vibrations of crystalline H_2O (symmetric and antisymmetric, ν_s H_2O and ν_{as} H_2O) in $Mg(ClO_4)_2 \cdot 6H_2O$, resulting in one new peak at the lowest experimental temperature with a maximum at 3280 cm^{-1}. All the other bands change with temperature as well, and mostly their intensity ratios alter. A typical example is the band at 1645 cm^{-1} consisting of at least three different vibrational modes (ammonium antisymmetric bending mode [δ_{as} NH_3^+], bending vibrations of the crystalline H_2O [δH_2O], and antisymmetric stretching of the carboxylic [ν_{as} COO^-] group). The peak intensities of the carboxylic anion bending (δ COO^-, 695 cm^{-1}) and its wagging mode (ω COO^-, 615 cm^{-1}) also change with temperature. They are more intense at 260 K compared to lower temperatures, while the signal of the twisting of the methylene group (*tw* CH_2, at 1315 cm^{-1}) and the shoulder at 1385 cm^{-1}, which belongs to a common peak of the methylene bending (δ CH_2) and carboxylic symmetric stretching vibration (ν_s COO^-), become more intense at 10 K compared to higher

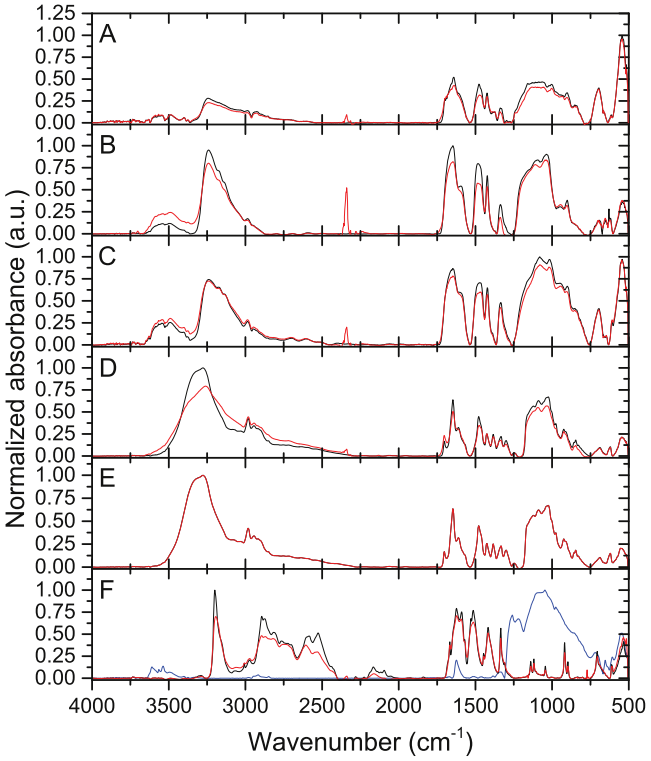

Figure 2. Infrared spectra of glycine–$Mg(ClO_4)_2 \cdot 6H_2O$ before (black line) and after irradiation (red line) at 260 K (A), 210 K (B), 160 K (C), and 10 K (D), along with the 10 K blank experiment (without irradiation, E), compared to pure glycine (black and red lines represent before and after irradiation, respectively) and pure $Mg(ClO_4)_2 \cdot 6H_2O$ (blue line) experiments at 10 K (F).

experimental temperatures. The signal from CO_2 (antisymmetric stretching, ν_{as} CO_2, 2340 cm^{-1}) forming upon irradiation also shows a temperature dependence: the rate at which its intensity increases with time is faster at elevated temperatures (Section 4.1). As for the pure glycine samples, the same holds true for the glycine–$Mg(ClO_4)_2 \cdot 6H_2O$ mixtures; smaller differences between intensity ratios and frequencies can also be due to small variances in thickness and unevenness of the sample.

4. DISCUSSION

4.1. Glycine Destruction Rates

When irradiating with energetic electrons, the absorptions associated with glycine and glycine–$Mg(ClO_4)_2 \cdot 6H_2O$ mixtures decrease; the rate of the decomposition depends on the temperature. Experimental decay curves of selected absorption peaks associated with glycine were extracted (Figures 3, 4). These decays were modeled with a first-order radiolytic decay of the samples using the following equation:

$$I(t) = I(0)e^{-k_i t}, \quad (1)$$

with $I(t)$ being the integrated IR intensity at time t (s), $I(0)$ the initial integrated IR intensity, and k_i the rate constant of the ith mode (s^{-1}). The decay rates of glycine have been determined by calculating and averaging the decay rates of two selected peaks, namely, the symmetric stretching vibration of the carboxylic anion (ν_s COO^- at 1410 cm^{-1}) and the ammonium symmetric bending (δ_s NH_3^+, 1500 cm^{-1}) of the zwitterionic glycine. Both peaks were extensively exploited to determine glycine decomposition rates (ν_s COO^-: Maté et al. 2011, 2014, 2015; Gerakines et al. 2012; Gerakines & Hudson 2013; Poch et al. 2013; δ_s NH_3^+: Poch et al. 2013) as they are high-intensity absorptions and barely overlap with bands of other vibrational modes; this makes them perfect candidates to ascertain the decay rates of glycine.

This procedure determined decay rates for pure glycine (in units of s^{-1}) of $(1.67 \pm 0.03) \times 10^{-4}$, $(2.58 \pm 0.15) \times 10^{-4}$, $(2.63 \pm 0.15) \times 10^{-4}$, and $(2.51 \pm 0.29) \times 10^{-4}$ at 10, 160, 210, and 260 K, respectively. For the glycine–$Mg(ClO_4)_2 \cdot 6H_2O$ mixtures, the rates were determined to be $(3.32 \pm 0.22) \times 10^{-4}$, $(3.77 \pm 0.28) \times 10^{-4}$, $(4.50 \pm 0.19) \times 10^{-4}$, and $(4.40 \pm 0.39) \times 10^{-4}$ s^{-1}, as summarized in Table 5. The decomposition rates depict a strong dependence: at 10 K, glycine is destroyed more slowly by at least 25%–30% than at higher temperatures ($k = 1.67$ vs. 2.51×10^{-4} for pure glycine at 10 and 260 K, respectively); however, for the high-temperature regime from 160 to 260 K, the destruction rates are nearly invariant on the temperature. This is especially valid for the pure glycine samples, for which the difference in the decay rates at 160, 210, and 260 K is less than 5% ($k = 2.58 \times 10^{-4}$ s^{-1} vs. 2.51×10^{-4} s^{-1}at 160 and at 260 K).

Most importantly, ClO_4^- addition to glycine has a significant influence on the destruction rates of glycine at all temperatures: the addition of ClO_4^- accelerates the degradation at all temperatures. Ratios for rates of destruction of the glycine–$Mg(ClO_4)_2 \cdot 6H_2O$ mixture and of the pure glycine samples were calculated for different experimental temperatures (Table 5); the results show that the presence of ClO_4^- accelerates the decomposition of glycine by 73% ± 27% ($(2.51 \pm 0.29) \times 10^{-4}$ s^{-1} for pure glycine vs. $(4.40 \pm 0.39) \times 10^{-4}$ s^{-1} for glycine–$Mg(ClO_4)_2 \cdot 6H_2O$ at 260 K). Turner et al. (2015b) investigated the radiolytic decomposition of ClO_4^- and concluded that, when samples of $Mg(ClO_4)_2 \cdot 6H_2O$ were irradiated with energetic electrons, ClO_4^- units decompose to chlorates (ClO_3^-) and atomic oxygen (O), the latter of which later combines with a second oxygen atom to form molecular oxygen (O_2). Since nascent oxygen (O) represents a highly reactive oxidizer, our results propose that, if an organic compound is present, two separate mechanisms degrade the organic molecules: reactions with the oxygen atoms and the radiolysis of the organic molecules. This results in an enhanced degradation of glycine in the presence of ClO_4^- at all temperatures from 10 to 260 K, as verified experimentally in this work. Most importantly, this ratio of the degradation of glycine–$Mg(ClO_4)_2 \cdot 6H_2O$ versus glycine of about two is invariant on the temperature. This is in accordance with the recent findings of Gerakines & Hudson (2015), who concluded that the higher destruction rates of glycine in CO_2 ice compared to those in H_2O ice can be explained by the formation of reactive radiolysis products (such as O atoms) generated by the irradiation of CO_2.

4.2. Carbon Dioxide and Carbon Monoxide Formation Rates

Eventually, the final oxidation products of organic molecules are CO_2 and CO. Here, their elevated production rates in the glycine–$Mg(ClO_4)_2 \cdot 6H_2O$ mixtures compared to experiments performed with pure glycine by a factor of about three and five, respectively, also verify the increased decomposition rate of glycine if ClO_4^- is present in the sample (Table 5). Note that the CO_2 and CO formation rates are about one order of magnitude lower than the destruction rates of glycine; this might indicate additional competing reaction pathways, which

Table 4
Infrared Absorptions for Glycine–$Mg(ClO_4)_2 \cdot 6H_2O$ and Radiation-induced Changes

Assignment[a,b]	260 K				210 K			
	Band Position (cm^{-1})[c]		Signal Strength[d]	Change upon Irrad.[e]	Band Position (cm^{-1})[c]		Signal Strength[d]	Change upon Irrad.[e]
	Before Irrad.	After Irrad.			Before Irrad.	After Irrad.		
$\nu_{s,as}$ OH[f]	3555.0, 3486.1	3555.0, 3486.1	m	0?	3540.0, 3487.1	3540.0, 3487.1	m	–
ν_{as} NH_3^+	3245.9, 3171.5sh	3238.7, 3171.5sh	s	–, b(+)	3241.0, 3176.0sh, 3137.4sh	3241, 3176.0, 3137.4	s	–, b(+)
ν_{as} CH_2, ν_s CH_2	2983.4	2983.4	sh	–	2986.5	2986.5	sh	–
ν_{as} CO_2[g]	⋯	2339.9	w	+	⋯	2339.4	w	+
δ_{as} NH_3^+, β OH[f], ν_s COO^-	1700.4sh, 1644.9, 1596.0sh	1700.4sh, 1644.9, 1596.0sh	s, b	–, b(+)	1701.3sh, 1679.8sh, 1645.4, 1586.7sh	1701.3sh, 1679.8sh, 1645.4, 1586.7sh	s, b	–, b(+)
δ_s NH_3^+	1477.5	1477.5	s, b	–	1479.5	1479.5	s, b	–, b(+)
δ CH_2, ν_s COO^-	1424.9, 1388.1sh, 1374.1sh	1424.9, 1388.1sh, 1374.1sh	s	–, b(+)	1421.9	1421.9	s	–, b(+)
ω CH_2	1338.3	1338.3	sh	–, b(+)	1339.0	1339.0	m	–
tw CH_2	1328.0	1328.0	m	–, b(+)	1314.8	1314.8	sh	–
ρ NH_3^+, ν_{as} ClO_4^-	1161.6	1161.6	s, vb	–	1139.1	1139.1	s, vb	–
ν_{as} ClO_4^-	1109.4	1109.4	s, b	–	1090.0	1090.0	s, vb	–
ν CN, ν_s ClO_4^-	1054.6, 1003.3	1054.6, 1003.3	s, b	–	1046.5, 1016.6sh	1046.5, 1016.6sh	s, vb	–
ρ CH_2, ν CC	901.2	901.2	m	–	900.2	900.2	m	–
δ COO^-	696.2	696.2	m, b	–	690.0	690.0	m, b	0
ω COO^-	615.6	615.6	w	0?	620.0	620.0	m, b	0
δ CCO^-, δ ClO_4^-	544.5	544.5	m, b	0?	542.7	542.7	m, b	0
$\nu_{s,as}$ OH[f]	3545.5, 3487.7	3545.5, 3487.7	w, b	(+)	3374.1, 3332.2	3374.1, 3332.2	s, b	–, b(+)
ν_{as} NH_3^+	3238.2, 3167.7sh, 3138.1sh	3238.2, 3167.7, 3138.1	s, b	–, b(+)	3278.8, 3173.2sh, 3079.9sh	3263.4, 3173.2sh, 3079.9sh	s, b	–, b(+)
ν_{as} CH_2, ν_s CH_2	2986.1	2986.1	w	–	2983.3	2983.3	w	–
ν_{as} CO_2[g]	⋯	2340.3	w	+	⋯	2341.7	w, b	+
δ_{as} NH_3^+, β OH[f], ν_{as} COO^-,	1647.7, 1582.2	1647.7, 1582.2	s, vb	–, b(+)	1703, 1660.1sh, 1646.9, 1610.5, 1562.4sh,	1703, 1660.1sh, 1646.9, 1610.5sh, 1562.4sh	m	–, b(+)
δ_s NH_3^+	1475.0	1475.0	s, b	–, b(+)	1480.9, 1463.4sh	1476.4, 1463.4sh	s	–, b(+)
δ CH_2, ν_s COO^-	1422.1, 1388.8sh	1422.1, 1388.8sh	s, b	–, b(+)	1428.8, 1422.1sh, 1385.0	1428.8, 1422.1sh, 1385.0	m	–
ω CH_2	1333.7	1333.7	s, b	–, b(+)	1344.1, 1332.5sh	1344.1, 1332.5sh	m	–, b(+)
tw CH_2	1309.9	1309.9	sh	–	1299.1	1299.1	m	–
ρ NH_3^+, ν_{as} ClO_4^-	1139.9, 1116.3	1139.9, 1116.3	s, b	–	1139.4sh, 1122.1	1139.4sh, 1122.1	s, vb	–, b(+)
ν_{as} ClO_4^-	1080.2	1080.2	s, b	–	1088.7, 1055.7sh	1091.8, 1055.7sh	s, vb	–
ν CN	1018.9	1018.9	s, b	–	1038.5sh, 1024.9	1035.3	s, vb	–
ν_s ClO_4^-[h]					1001.3sh, 975.2	1001.3sh, 975.2	w, vb	–
ρ CH_2	900.2	900.2	s, b	–	923.9, 908.2sh	923.9, 908.2sh	m, b	–

Table 4
(Continued)

Assignment[a,b]	260 K				210 K			
	Band Position (cm^{-1})[c]				Band Position (cm^{-1})[c]			
	Before Irrad.	After Irrad.	Signal Strength[d]	Change upon Irrad.[e]	Before Irrad.	After Irrad.	Signal Strength[d]	Change upon Irrad.[e]
ν CC[h]					883.1sh	883.1sh	sh	–
δ COO^-	696.0	696.0	m, b	0	689.1	689.1	m, b	0?
ω COO^-	609.9	609.9	w	0	632.6, 621.0	632.6, 621.0	m	0?
δ CCO^-, δ ClO_4^-	544.8	544.8	m, b	0	541.5	541.5	m, b	–

Notes.
[a] Assignments based on previous experimental studies (for glycine see Table 3; $Mg(ClO_4)_2 \cdot 6H_2O$, Miller & Wilkins 1952; Bishop et al. 2014; Hanley et al. 2015).
[b] ν: Stretching, δ: bending, ω: wagging, tw: twisting, ρ: rocking, s: symmetric, as: antisymmetric vibrations.
[c] ⋯: no signal, sh: shoulder, w: weak band.
[d] s: Strong, m: medium, (v)w: (very) weak, sh (shoulder), (v)b: (very) broad band.
[e] −: band decreases, +: band increases, 0: no change, b: broadening, b(+): broadening with possible new bands upon irradiation. ?: uncertain.
[f] Vibrations of crystalline H_2O in $Mg(ClO_4)_2 \cdot 6H_2O$.
[g] Stretching vibration of irradiation product CO_2.
[h] The two vibrational modes can be distinguished at 10 K.

may account for the majority of glycine depletion (Section 4.2). It is important that we only report the rate constants for CO_2 formation at 10 K. Note that CO_2 was found to effectively diffuse out of the irradiated samples at elevated temperatures of 160 K and higher; therefore, the IR spectroscopically detected CO_2 and hence the temporal plots at higher temperatures do not represent the complete CO_2 and CO balances. However, at 10 K, CO_2 and CO are trapped within the ice. One also has to consider the possibility that some of the CO may originate from the radiolysis of CO_2, in which the latter forms and decomposes simultaneously (Bennett et al. 2004; Bennett & Kaiser 2007; Bennett et al. 2010). Exploiting a consecutive reaction mechanism ($A \rightarrow B \rightarrow C$), where A denotes glycine, B depicts CO_2, and C represents CO, the following equations can be deduced for fitting the evolution of CO_2 and CO with time (Bennett & Kaiser 2005):

$$I(CO_2, t) = I(0)\frac{k_1}{k_2 - k_1}(e^{-k_1 t} - e^{-k_2 t}), \quad (2)$$

$$I(CO, t) = I(0)\left[1 - \frac{k_2}{k_2 - k_1}e^{-k_1 t} + \frac{k_1}{k_2 - k_1}e^{-k_2 t}\right], \quad (3)$$

where $I(t)$ is the integrated IR intensity of a given species at time t (in s), $I(0)$ is the integrated IR intensity of parent molecule glycine at the beginning of irradiation, and k_1 and k_2 are the formation rate constants of CO_2 and CO (in s^{-1}), respectively.

This kinetic fit reveals fundamental differences between the formation rates of CO_2 and CO in pure glycine, $k_1 = (0.14 \pm 0.01) \times 10^{-4}\,s^{-1}$ and $k_2 = (0.12 \pm 0.01) \times 10^{-4}\,s^{-1}$, and in glycine–$Mg(ClO_4)_2 \cdot 6H_2O$ samples, $k_1 = (0.39 \pm 0.07) \times 10^{-4}\,s^{-1}$ and $k_2 = (0.56 \pm 0.07) \times 10^{-4}\,s^{-1}$, at 10 K, once again with CO_2 and CO forming faster by a factor of five and three in mixtures containing ClO_4^-. This indicates that the oxygen atoms released in the radiolysis of ClO_4^- (Turner et al. 2015b) have a dramatic effect on the destruction rates of glycine and the formation rates of the degradation products (CO_2 and CO) and hence accelerate these rates by factors between two and five at 10 K. More specifically, the formation rate of CO originating from the decomposition of CO_2 (k_2) is similar to the values determined by previous works studying the irradiation of CO_2 ices with energetic electrons in an identical setup at 10 K (Bennett et al. 2010). However, if ClO_4^- is also present, the CO formation rate rises by a factor of up to five to $(0.56 \pm 0.07) \times 10^{-4}\,s^{-1}$.

4.3. Temperature-dependent Rate Constants (Glycine Destruction)

Let us focus our attention now on the temperature dependence of the glycine destruction rates (Figure 5). The temperature dependence of a rate constant for a chemical reaction can be expressed by the Arrhenius equation:

$$k(T) = e^{-\Delta G^{\ddagger}/RT}, \quad (4)$$

where $k(T)$ is the reaction rate in s^{-1}, A the so-called pre-exponential factor (s^{-1}), $\Delta G^{\ddagger}$ the classical activation energy in J mol^{-1}, R the gas constant (8.314 J mol^{-1} K^{-1}), and T the temperature in K. Fitting this equation to the rate constants as compiled in Table 5, activation energies of only 39 ± 1 J mol^{-1} for pure glycine and 23 ± 10 J mol^{-1} for the glycine–$Mg(ClO_4)_2 \cdot 6H_2O$ mixture were determined. Considering that any bond-breaking process taking place in glycine is endoergic (for instance, the dissociation energy of its C–C bond is 349 ± 1 kJ mol^{-1}; Luo 2007), there seems to be a discrepancy between the energy required for bond breaking and the experimentally determined activation energies. This apparent inconsistency can be resolved if we take into account that the radiolysis-induced bond cleavage represents a non-equilibrium process. These processes are inherently temperature independent (Morton & Kaiser 2003), and the kinetic energy of the energetic electrons exceeds the energy necessary to cleave the chemical bonds. In spite of this, a small

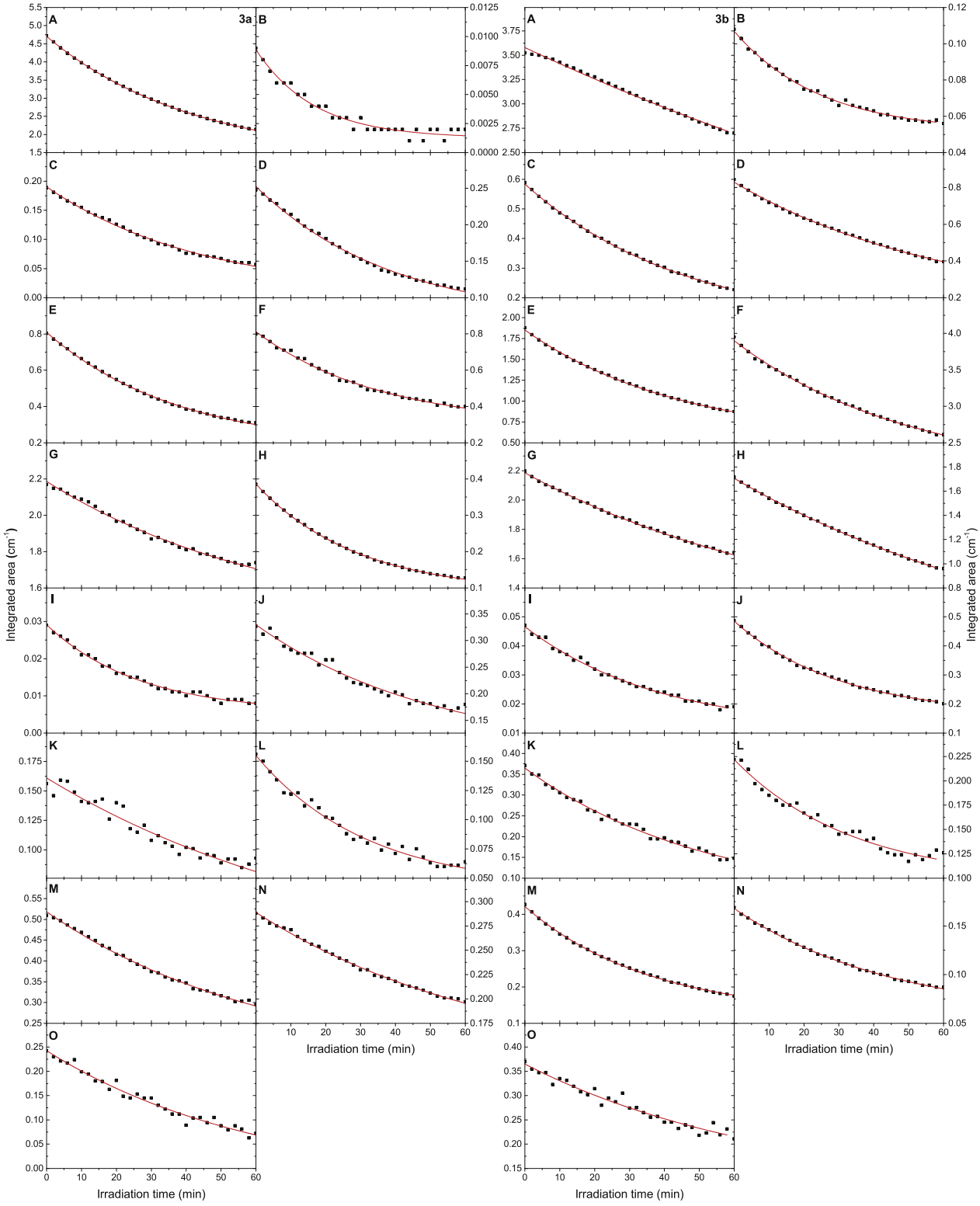

Figure 3. Decay curves determined from integrated areas of the IR bands of glycine film upon irradiation at 260 K (3a, left graph), 210 K (3b, right graph) 160 K (3c, left graph on next page), and 10 K (3d, right graph on next page), respectively. Band positions for 3a are 3174.8 cm^{-1} (A), 3009.8 cm^{-1} (B), 2979.2 cm^{-1} (C), 1662.0 cm^{-1} (D), 1619.7, 1593.2 cm^{-1} (E), 1525.6, 1512.5 cm^{-1} (F), 1433.0, 1396.7 cm^{-1} (G), 1336.8 cm^{-1} (H), 1309.9 cm^{-1} (I), 1137.9 cm^{-1} (J), 1118.3 cm^{-1} (K), 1043.5 cm^{-1} (L), 918.0 cm^{-1} (M), 896.8 cm^{-1} (N), and 611.6 cm^{-1} (O). Band positions for 3b are 3187.3 cm^{-1} (A), 3008.3 cm^{-1} (B), 2976.8 cm^{-1} (C), 1662.9 cm^{-1} (D), 1639.4, 1591.7 cm^{-1} (E), 1506.1, 1493.8 cm^{-1} (F), 1443.9, 1404.5 cm^{-1} (G), 1334.5 cm^{-1} (H), 1309.0 cm^{-1} (I), 1137.6 cm^{-1} (J), 1117.1 cm^{-1} (K), 1043.1 cm^{-1} (L), 914.7 cm^{-1} (M), 897.8 cm^{-1} (N), and 613.6 cm^{-1} (O). Decay curves determined from integrated areas of the IR bands of glycine film upon irradiation at 160 K (3c, left graph) and 10 K (3d, right graph). Band positions for 3c are 3175.9 cm^{-1} (A), 3007.9 cm^{-1} (B), 2981.2 cm^{-1} (C), 1664.9 cm^{-1} (D), 1641.6, 1594.8 cm^{-1} (E), 1511.5, 1493.8 cm^{-1} (F), 1440.7, 1400.8 cm^{-1} (G), 1336.7 cm^{-1} (H), 1308.5 cm^{-1} (I), 1138.0 cm^{-1} (J), 1117.5 cm^{-1} (K), 1044.7 cm^{-1} (L), 915.4 cm^{-1} (M), 898.5 cm^{-1} (N), and 613.9 cm^{-1} (O). Band positions for 3d are 3201.1 cm^{-1} (A), 3008.4 cm^{-1} (B), 2973.8 cm^{-1} (C), 1667.5 cm^{-1} (D), 1624.4, 1588.8 cm^{-1} (E), 1529.4, 1514.5 cm^{-1} (F), 1446.8, 1417.5 cm^{-1} (G), 1335.8 cm^{-1} (H), 1309.4 cm^{-1} (I), 1140.4 cm^{-1} (J), 1119.6 cm^{-1} (K), 1044.5 cm^{-1} (L), 918.1 cm^{-1} (M), 896.8 cm^{-1} (N), 611.9 cm^{-1} (O), the increasing CO_2 band at 2339.4 cm^{-1} (P), and the CO band at 2131 cm^{-1} (Q).

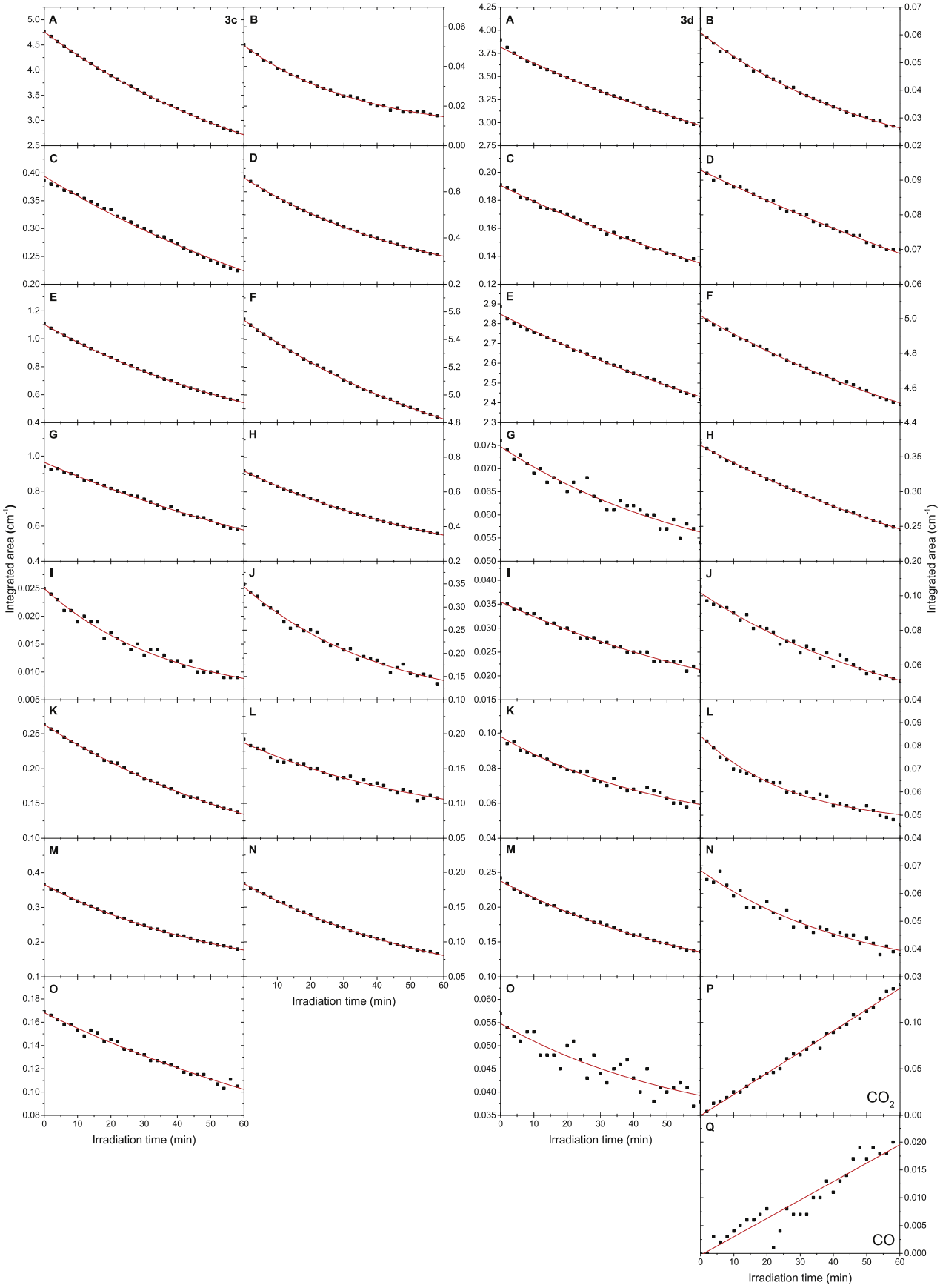

Figure 3. (Continued.)

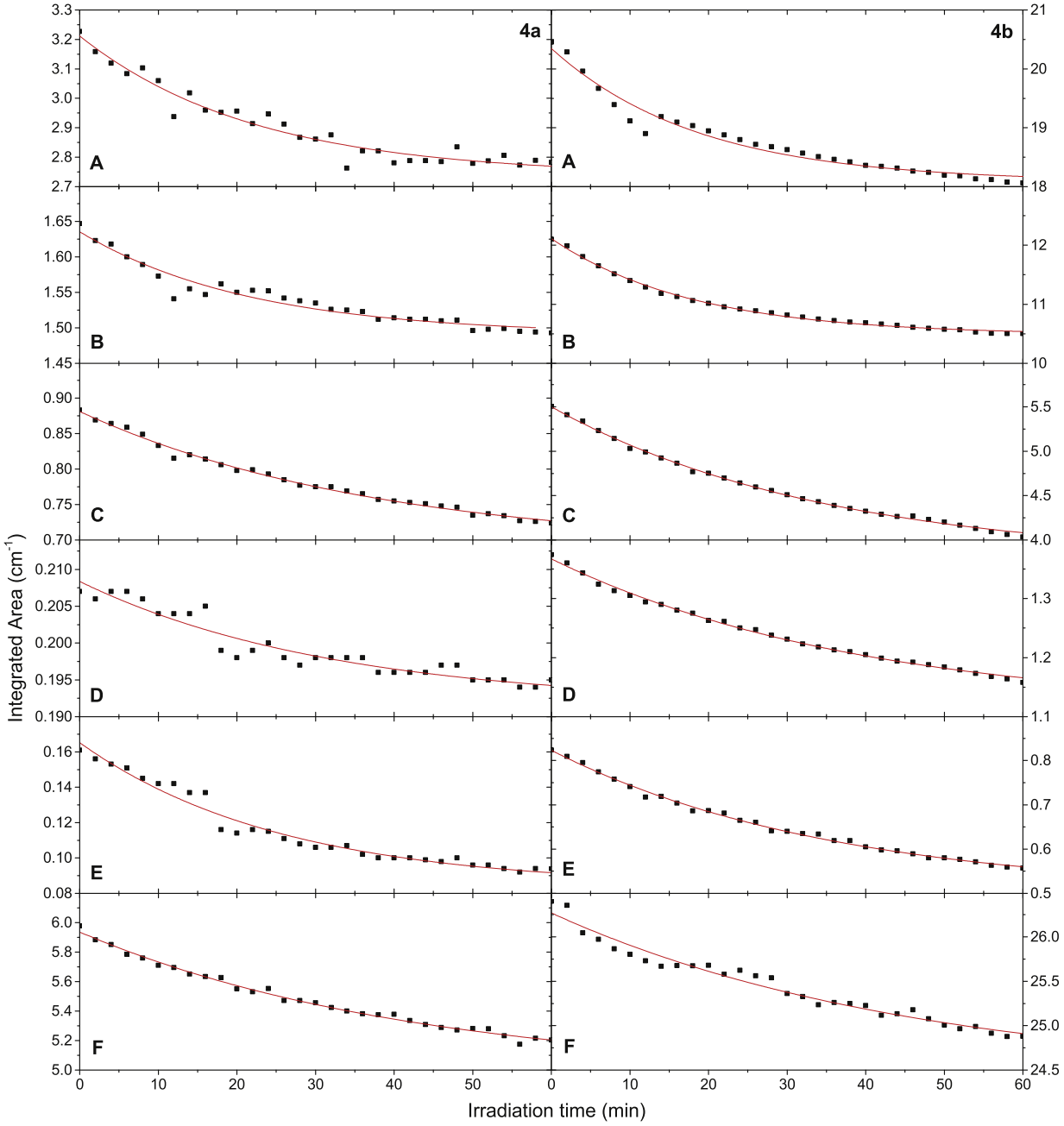

Figure 4. Decay curves determined from integrated areas of the IR bands of the glycine–$Mg(ClO_4)_2 \cdot 6H_2O$ 1:1 mixture film upon irradiation at 260 K (4a, left panel), 210 K (4b, right panel) 160 K (4c, left panel on next page), and 10 K (4d, right panel on next page), respectively. Band positions for 4a are 3245.9 cm^{-1} (A), 1644.9, 1596.0 cm^{-1} (B), 1477.5 cm^{-1} (C), 1424.9 cm^{-1} (D), 1338.3, 1328.3 cm^{-1} (E), the broad band in the region of 1265–790 cm^{-1} (F), and the increasing CO_2 band at 2338.8 cm^{-1} (G). Band positions for 4b are 3241.0 cm^{-1} (A), 1645.4, 1586.7 cm^{-1} (B), 1479.5 cm^{-1} (C), 1421.9 cm^{-1} (D), 1339.0, 1314.8 cm^{-1} (E), and the broad band in the region of 1265–765 cm^{-1} (F). Decay curves determined from integrated areas of the IR bands of glycine–$Mg(ClO_4)_2 \cdot 6H_2O$ 1:1 mixture film upon irradiation at 160 K (4c, left panel) and 10 K (4d, right panel). Band positions for 4c are 3238.2 cm^{-1} (A), 1647.7, 1582.2 cm^{-1} (B), 1475.0 cm^{-1} (C), 1422.1 cm^{-1} (D), 1333.7, 1309.9 cm^{-1} (E), the broad band in the region of 1260–760 cm^{-1} (F), and the increasing CO_2 band at 2340.3 cm^{-1} (G). Band positions for 4d are 3278.8 cm^{-1} (A), 1660.1, 1610.5 cm^{-1} (B), 1480.9 cm^{-1} (C), 1428.8 cm^{-1} (D), 1344.1, 1299.1 cm^{-1} (E), the broad band in the region of 1210–755 cm^{-1} (F), the increasing CO_2 band at 2341.7 cm^{-1} (G), and CO band at 2131 cm^{-1} (H).

temperature dependency of the reaction is still observable. This might be attributed to a diffusion-limited reaction: the products formed have to diffuse from each other to prevent a possible reverse reaction to "recycle" the parent molecule. The activation energies for glycine and glycine–$Mg(ClO_4)_2 \cdot 6H_2O$ ($\Delta G^{\ddagger} = 39 \pm 1$ J mol^{-1} and 23 ± 10 J mol^{-1}, respectively) are in the classical range of activation energies in diffusion-limited reactions; for comparison, these energies are a factor of typically five higher than that observed for the lighter deuterium atoms (D) and molecules (D_2, $\Delta G^{\ddagger} \approx 3$–$7$ J mol^{-1}, He et al. 2010) in irradiated CD_4 ices at 10 K.

4.4. Mass Balances

The number of degraded glycine molecules in the pure samples can also be evaluated both for the pure glycine sample and for the glycine–$Mg(ClO_4)_2 \cdot 6H_2O$ mixture. Based on the

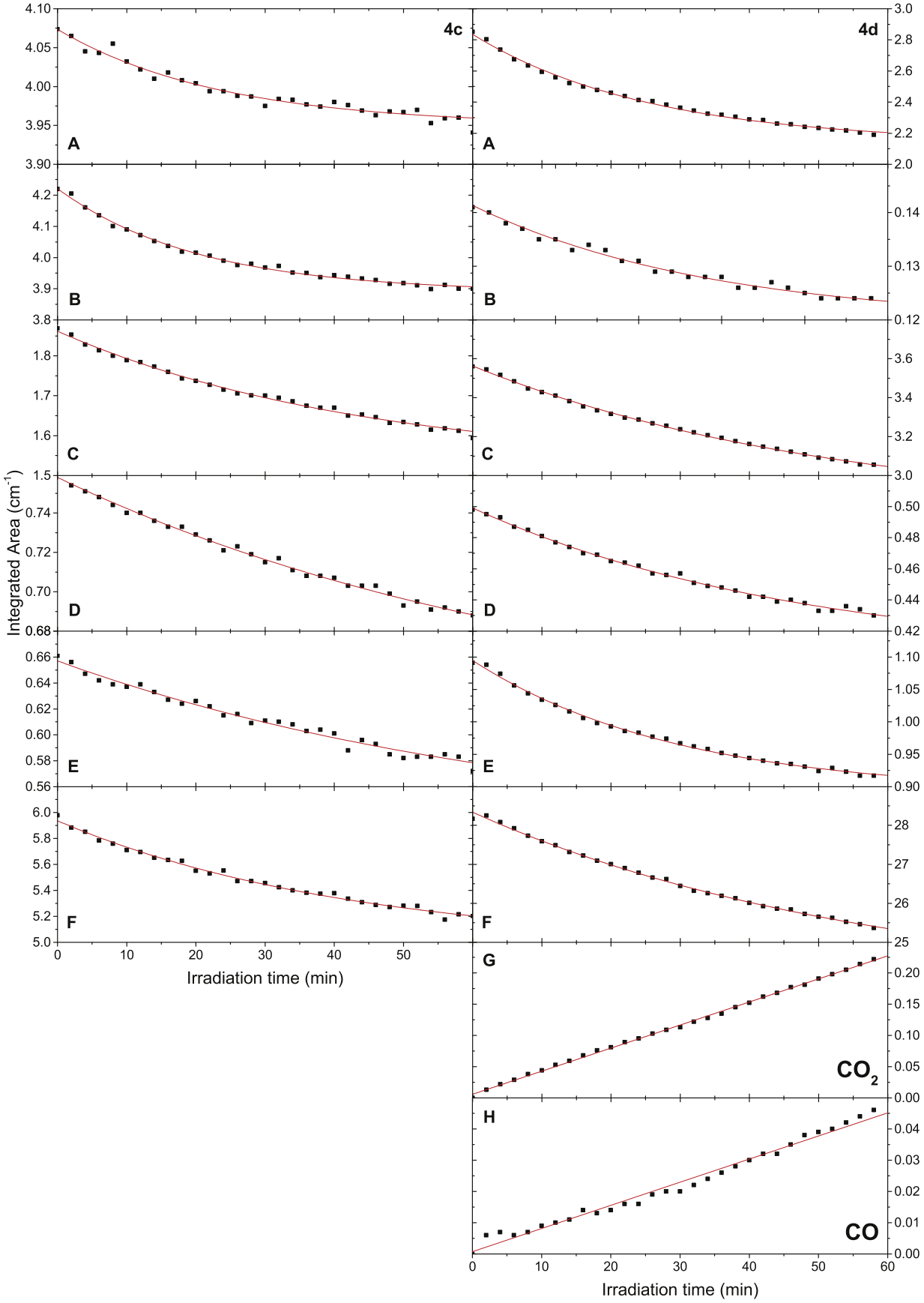

Figure 4. (Continued.)

Table 5
Rate Constants (in 10^{-4} s^{-1}) of Glycine Destruction in Glycine and Glycine–$Mg(ClO_4)_2 \cdot 6H_2O$ Mixtures upon Radiolysis and Production Rates of CO_2 and CO

Temperature (K)	Glycine	Glycine–Mg $(ClO_4)_2 \cdot 6H_2O$ Mixture	Ratio of k(Mixture) and k (Glycine)
260	2.51 ± 0.29	4.40 ± 0.39	1.8 ± 0.3
210	2.63 ± 0.15	4.50 ± 0.19	1.7 ± 0.3
160	2.58 ± 0.15	3.77 ± 0.28	1.5 ± 0.3
10	1.67 ± 0.03	3.32 ± 0.22	2.0 ± 0.4
CO_2 formation rate (10 K)	0.14 ± 0.01	0.39 ± 0.07	2.8 ± 0.6
CO formation rate (10 K)	0.12 ± 0.01	0.56 ± 0.07	4.7 ± 1.0

density (1.61 ± 0.01 g cm^{-3}), molar mass (75.06 g mol^{-1}), and thickness of the sample (480 ± 60 nm), the total number of molecules in the glycine sample is (1.98 ± 0.46) × 10^{18}. Furthermore, as the average electron penetration depth is 277 ± 55 nm, (1.15 ± 0.37) × 10^{18} molecules are exposed according to the CASINO simulation (Table 2). It should be emphasized that, since the dose absorbed by the molecules is relatively low (9.4 ± 0.2 eV), only a fraction of the exposed molecules decay, and the estimated number of decomposed glycine molecules should also be evaluated. Once again, this is conducted only at 10 K since the low target temperature presents an "outgassing" of the radiolysis products. The ratio of the integrated IR band areas after and before the irradiation is determined and corrected for the ratio of the exposed sample molecules, taking into account the sample thickness and the penetration depth of the electrons. Here, the number of destroyed glycine molecules is determined to be (6.51 ± 0.16) × 10^{17}, which equals 57% of the exposed molecules.

From the integrated band areas of forming CO_2 (ν_{as} CO_2, 2340 cm^{-1}) and CO (νCO, 2131 cm^{-1}) and by exploiting their integrated absorption coefficients of 7.6 × 10^{-17} cm $molecule^{-1}$ and 1.1 × 10^{-17} cm $molecule^{-1}$, respectively (Gerakines et al. 1995), we determined their abundances in the sample after the irradiation to be (6.43 ± 0.03) × 10^{15} and (7.36 ± 2.21) × 10^{15}, respectively (Table 6) (Turner et al. 2015). Assuming that CO originates from the radiolysis of CO_2 and that one glycine molecule yields a single CO_2 molecule upon radiolysis (Reaction (R1)), or

$$^{+}H_3NCH_2COO^{-} \rightarrow CH_3NH_2 + CO_2, \qquad (R1)$$

we can determine the total number of glycine molecules that would be needed to explain the CO_2 and CO abundances after the irradiation to be (1.38 ± 0.28) × 10^{16}. However, considering that (6.51 ± 0.16) × 10^{17} glycine molecules decomposed, but only (1.38 ± 0.28) × 10^{16} can be accounted for by the newly formed CO_2 and CO molecules (i.e., only 2.1% ± 0.5%), it is evident that alternative degradation pathways—as proposed in the aforementioned discussion—of glycine must exist. These could be polymerization reactions (Kaiser et al. 2013; Pilling et al. 2013), which might play a major role in the destruction of glycine, or alternative decomposition pathways as discussed below.

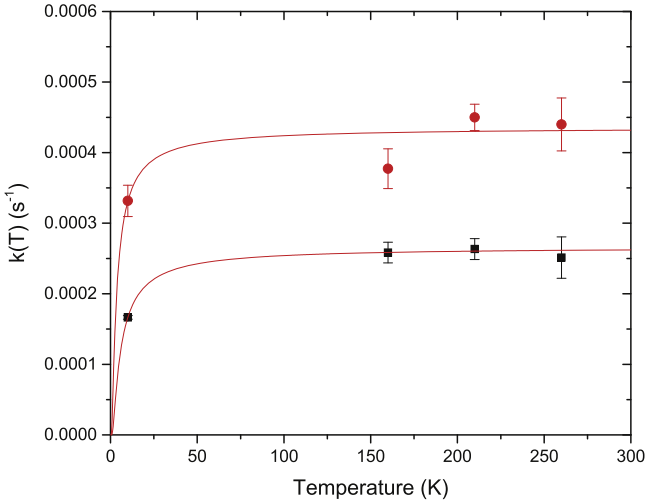

Figure 5. Rate constant (k) vs. temperature (T) plot of the decomposition of glycine in pure glycine (black squares) and glycine–$Mg(ClO_4)_2 \cdot 6H_2O$ (red circles) samples.

As for the glycine–$Mg(ClO_4)_2 \cdot 6H_2O$ mixture, based on the average density (1.80 ± 0.19 g cm^{-3}), average molar mass (203.2 g mol^{-1}), thickness of the sample (530 ± 60 nm), and the calculated average penetration depths (253 ± 51 nm) using the CASINO simulation, (2.16 ± 0.97) × 10^{17} glycine molecules are exposed from the total number of (4.51 ± 1.41) × 10^{17} when irradiated with the electrons, along with the same number of $Mg(ClO_4)_2 \cdot 6H_2O$ molecules because they are in an equimolar mixture. The number of decomposed glycine molecules can be determined by using the aforementioned method, giving (1.67 ± 0.55) × 10^{17}; this results in 77% of the exposed molecules. This means that the number of decomposed molecules in the glycine–$Mg(ClO_4)_2 \cdot 6H_2O$ mixture increased compared to the pure glycine sample (57%); the enhanced radiolysis of glycine in the glycine–Mg $(ClO_4)_2 \cdot 6H_2O$ mixture correlates with the difference in degradation rates discussed above (see Tables 5 and 6).

The number of CO_2 and CO molecules formed is (9.73 ± 0.49) × 10^{15} and (9.02 ± 0.72) × 10^{15}, respectively; the number of released CO_2 molecules is 5.4% ± 2.4% of the total number of destroyed glycine molecules ((1.67 ± 0.55) × 10^{17}), depicting a more efficient destruction of organic molecules in the presence of ClO_4^-. These two species can account for a total of (1.88 ± 0.28) × 10^{16} glycine molecules being degraded, or 11% ± 6% of the glycine.

Most importantly, ClO_4^- can also be radiolyzed. Turner et al. (2015b) derived that (8.0 ± 2.5) × 10^{-3} O atoms are formed when a $Mg(ClO_4)_2 \cdot 6H_2O$ molecule absorbs 1 eV energy on average. Considering our dose of 36 ± 1 eV per $Mg(ClO_4)_2 \cdot 6H_2O$ unit and the number of exposed units in our sample ((2.16 ± 0.97) × 10^{17}), (6.25 ± 3.95) × 10^{16} O atoms were released. These O atoms can react with the glycine molecules as well, thus accelerating the degradation of glycine, as elucidated above (Table 5). If we consider the relative increase in glycine decomposition with ClO_4^- and when it is not present in the sample (77% vs. 57%), one can see that the difference can be related to the presence of oxygen atoms. Specifically, the difference between the 77% ((1.67 ± 0.55) × 10^{17}) and 57% ((1.23 ± 0.41) × 10^{17}) of the

Table 6
Degraded Glycine and Newly Formed Molecules at 10 K

Process	Decay product	Number of Molecules Produced/Decomposed during Irradiation	
		Glycine	Glycine–$Mg(ClO_4)_2 \cdot 6H_2O$
$^+H_3NCH_2COO^- \rightarrow$ X		$(6.51 \pm 0.16) \times 10^{17}$	$(1.67 \pm 0.55) \times 10^{17}$
Fraction of glycine degraded		57%	77%
$ClO_4^- \rightarrow ClO_3^- + O$	O	...	$(6.95 \pm 1.56) \times 10^{16}$[a] $(6.25 \pm 3.95) \times 10^{16}$[b]
	CO_2	$(6.43 \pm 0.03) \times 10^{15}$	$(9.73 \pm 0.49) \times 10^{15}$
	CO	$(7.36 \pm 2.21) \times 10^{15}$	$(9.02 \pm 0.72) \times 10^{15}$
	Fraction[c]	$2.1 \pm 0.5\%$	$11 \pm 6\%$
Number of product molecules in sample after irradiation	CH_3NH_2	$(1.45 \pm 0.44) \times 10^{15}$	$(1.82 \pm 0.57) \times 10^{15}$
	CH_4	$<(2.69 \pm 1.35) \times 10^{15}$	$<(2.69 \pm 1.35) \times 10^{15}$
	NH_3	$(1.54 \pm 0.77) \times 10^{15}$	$(1.54 \pm 0.77) \times 10^{15}$
	Fraction[d]	$41 \pm 20\%$	$30 \pm 15\%$

Notes.
[a] Determined from experimental IR spectrum.
[b] Based on the results of Turner et al. (2015b).
[c] Fraction of CO_2 and CO that account for the decomposition of glycine via Reaction (R1) and radiolysis of CO_2 to CO.
[d] Fraction of reaction products of (R1) to (R3) accounting for CO_2 and CO.

exposed glycine molecules ($(2.16 \pm 0.97) \times 10^{17}$) in the glycine–$Mg(ClO_4)_2 \cdot 6H_2O$ mixture is equal to roughly 4.40×10^{16}, which is approximately 70% of the calculated number of O atoms produced during irradiation ($(6.25 \pm 3.95) \times 10^{16}$).

4.5. Other Decay Products

As pointed out in Sections 3.1 and 3.2, strong absorption peaks of CO_2 and CO could be identified unambiguously; a broadening of the IR bands can be observed as well when samples are irradiated with the energetic electrons. The latter phenomenon can be assigned to the formation of new products and also to an amorphization of crystalline glycine. In this section, we discuss which reaction products are likely responsible for the widening of the absorption features (Table 7). One of these candidates is CH_3NH_2, which is the decay product of zwitterionic glycine when CO_2 is formed during its decarboxylation reaction according to Reaction (R1). With a C–C bond dissociation energy of 349 ± 8 kJ mol^{-1} (3.62 eV) (Luo 2007), which is only one-third of the average energy dose of 9.4 and 10.1 eV absorbed per glycine molecule in the pure and $Mg(ClO_4)_2 \cdot 6H_2O$ mixtures, this reaction may account for the majority of the CO_2 formed during irradiation.

Despite the fact that none of the previous proton and electron irradiation works could detect CH_3NH_2 conclusively (Table 1), it could be observed during several UV irradiation experiments of glycine via IR spectroscopy (Maté et al. 2014). The fact that the absorption peaks of CH_3NH_2 lie close to the absorptions of glycine (Gerakines et al. 2012) makes its IR detection extremely difficult, and signals of the two compounds might be indistinguishable when the concentration of CH_3NH_2 is extremely low. Nevertheless, its signals can cause the broadening of the IR absorptions: stretching vibrations of its amino (ν NH_2, at 3295 cm^{-1}; Holtom et al. 2005) and antisymmetric methyl (ν_{as} CH_3, 3000, 2995, and 2951 cm^{-1}) groups, and bending modes of amino (δ NH_2, at roughly 1592 cm^{-1}) and methyl (symmetric: δ_s CH_3, 1508 and 1477 cm^{-1}, antisymmetric δ_{as} CH_3, 1411 cm^{-1}) groups, like twisting of amino (tw NH_2, 1357 cm^{-1}), rocking of methyl (ρ CH_3, 1149 cm^{-1}) groups, and C–N bond stretching (ν CN, at around 1036 cm^{-1}). Even if all broadening is only based on CH_3NH_2 formation, its concentration in the samples is extremely low after the irradiation ($(1.45 \pm 0.44) \times 10^{15}$ and $(1.82 \pm 0.57) \times 10^{15}$) in the pure and mixed samples, respectively; these data were determined by exploiting the absorption coefficient 4.3×10^{-18} cm molecule^{-1} of the 1592 cm^{-1} band (Holtom et al. 2005). Since a factor of about 10 less CH_3NH_2 is formed compared to what is expected based on Reaction (R1), the majority of CH_3NH_2 might undergo radiolysis to CH_4 and nitrene (NH) (Reaction (R2)) or NH_3 along with carbene (CH_2) (Reaction (R3)):

$$CH_3NH_2 \rightarrow CH_4 + NH \quad \text{(R2)}$$

$$CH_3NH_2 \rightarrow CH_2 + NH_3. \quad \text{(R3)}$$

Therefore, the broadening of the methylene stretching vibrations (ν_{as} CH_2 and ν_s CH_2) of glycine might be attributable to the presence of CH_4 antisymmetric stretching vibrations (ν_{as} CH_4) with a maximum at around 3009 cm^{-1} in the glycine–$Mg(ClO_4)_2 \cdot 6H_2O$ sample. Regarding our samples irradiated at 10 K, the antisymmetric stretching (ν_{as} NH_3) along with the symmetric bending vibration of NH_3 (δ_s NH_3) can be tentatively assigned to the widening of the broad absorption bands at around 3370 and 1100 cm^{-1}. Nevertheless, the concentration of these species is still very low ($<(2.69 \pm 1.35) \times 10^{15}$ and $(1.54 \pm 0.77) \times 10^{15}$) based on the absorption coefficient of the signal at 1103 cm^{-1} (1.2×10^{-17} cm molecule^{-1}; Gerakines et al. 2005). Consequently, the IR signal and species produced in Reactions (R1) to (R3) can only account for $41\% \pm 20\%$ and $32\% \pm 15\%$ of the CO_2 and CO formed in glycine and glycine–Mg $(ClO_4)_2 \cdot 6H_2O$ mixtures, respectively. Therefore, alternative hitherto-unidentified degradation pathways of CH_3NH_2 must still exist.

5. ASTROPHYSICAL IMPLICATIONS

Our primary goal was to investigate the radiolytic decomposition of glycine under simulated Mars conditions in the presence (and absence) of ClO_4^- anions, which are abundant

Table 7
Infrared Absorption Assignments for Possible Decay Products at 10 K

Decay Product	Assignment[a]	Literature Value[b]	Pure Glycine Experiment		Glycine–$Mg(ClO_4)_2 \cdot 6H_2O$ Mixture Experiment	
		Band Position (cm^{-1})	Observation[c]	Band Position (cm^{-1})[d]	Observation[c]	Band Position (cm^{-1})[d]
CO_2	$\nu_{as}\ CO_2 + \nu_s\ CO_2$[e]	3709	–	⋯	–	⋯
(Bennett et al. 2014)	$\nu_{as}\ CO_2 + \beta\ CO_2 \times 2$[e,f]	3601	–	⋯	–	⋯
	$\nu_{as}\ CO_2$	2339	+	2339	+	2340
	$\beta\ CO_2$	656	(+)	667	–?	⋯
CO (Bennett et al. 2009)	ν CO	2138	+	2131	+	2131
CH_3NH_2	$\nu\ NH_2$	3296	(+)	3293	(+)	3294
(Holtom et al. 2005)	$\nu_{as}\ CH_3$	3001	(+)	2999	(+)	3001
	$\nu_{as}\ CH_3$	2995	(+)	2993	(+)	2996
	$\nu_{as}\ CH_3$	2950	(+)	2948	(+)	2954
	$\nu_s\ CH_3$	2798	–?	⋯	–?	⋯
	$\delta\ NH_2$	1594	(+)	1593	(+)	1591
	$\delta_{as}\ CH_3$	1504	(+)	1506	(+)	1509
	$\delta_{as}\ CH_3$	1475	(+)	1479	(+)	1476
	$\delta_s\ CH_3$	1413	(+)	1407	(+)	1416
	tw NH_2	1357	(+)	1353	(+)	1361
	$\rho\ CH_3$	1167	–	⋯	–?	⋯
	$\rho\ CH_3$	1146	(+)	1149	–?	1149
	ν CN	1041	(+)	1037	(+)	1035
	$\omega\ NH_2$	820	–	⋯	–?	821
NH_3 (Zheng and Kaiser 2007)	$\nu_{as}\ NH_3$	3372	(+)	3375	(+)?	3376?
	$\delta_s\ NH_3$	1097	(+)	1103	(+)?	1103?
CH_4	$\nu_{as}\ CH_4$	3010	(+)	3011	(+)	3007
(Bennett et al. 2006)	$\omega\ CH_4$	1302	(+)	1303	–?	–?

Notes.
[a] ν: stretching, δ: bending, ω: wagging, tw: twisting, ρ: rocking, s: symmetric, as: antisymmetric vibrations.
[b] Assignments based on frequencies of previous studies given in parentheses.
[c] +: can be detected, –: cannot be detected, (+): tentative, possible presence. ?: uncertain.
[d] ⋯: no signal.
[e] Combination band.
[f] Overtone.

oxidizers on the surface of Mars (Hecht et al. 2009; Davila et al. 2013). Pure glycine and glycine–$Mg(ClO_4)_2 \cdot 6H_2O$ samples were irradiated with energetic electrons, which mimic secondary electrons originating from the interaction of GCRs and organics within the Martian regolith (Bennett et al. 2005; Bennett & Kaiser 2007). The measurements have been performed at four different temperatures (10, 160, 210, 260 K), and IR spectra have been taken online and in situ during the radiation exposure. The doses absorbed by pure glycine have been computed using a CASINO simulation and were found to be 9.4 ± 0.2 eV molecule^{-1}; the same values for the glycine–$Mg(ClO_4)_2 \cdot 6H_2O$ mixture are 10.1 ± 0.3 eV molecule^{-1} for glycine and 36.2 ± 1.0 eV molecule^{-1} for $Mg(ClO_4)_2 \cdot 6H_2O$. According to the calculations of Pavlov et al. (2012) and the measurements performed by the RAD instrument on board the Curiosity Rover (Hassler et al. 2014), these values correspond to a dose that a molecule that is 5–10 cm below the Martian surface absorbs roughly over 240 My, and the time needed for complete decomposition of glycine is offset by the supposed input rate of amino acids via meteoritic infall (15 ng m^2 yr^{-1}; ten Kate et al. 2005). However, Turner et al. (2015b) pointed out that ClO_4^- anions, which are abundant species on the surface of Mars, are also susceptible to high-energy irradiation, and their decay products, ClO_3^- and especially atomic O, may facilitate the degradation of glycine because the absolute formation rate of the latter ($(3.4 \pm 1.2) \times 10^{14}$ m^{-2} yr^{-1}) is higher than the yearly glycine influx (1.2×10^{14} m^{-2} yr^{-1}; ten Kate et al. 2005). In accordance with this, the results of our experiments clearly show that the presence of ClO_4^- does speed up the decomposition rate of amino acids, which possibly explains why organics can be found on the surface and subsurface of Mars only in trace amounts despite their continuous resupply via in situ formation and from interstellar sources.

The effect of ClO_4^- on the radiolysis of organics has not been studied so far, and the results of these measurements allow for several conclusions to be made. *First*, considering the Mars-relevant temperature range covering 160–260 K, the destruction rates of pure glycine and glycine mixed with ClO_4^- are nearly temperature invariant, with rates varying as little as 5% (Table 5). *Second*, the rate constants of the glycine decomposition in the presence of ClO_4^- were consistently a factor of about two higher than for pure glycine, suggesting that the energetic O atoms released from ClO_4^- have a significant

Table 8
Doses Glycine Exposed to in Previous Experiments

Reference	Type of Radiation, Energy (eV)	Dose (eV molecule^{-1})
ten Kate et al. (2005)	UV, 6.9–10.3 and 3.1–6.5	(12.5 ± 7.8) and (5.48 ± 1.55) × 10^{-5}
Poch et al. (2015)	UV, 3.1–6.5	(4.48 ± 1.28) × 10^{-3} [b]
Stoker & Bullock (1997)	UV, <5.9	(1.64 ± 0.47) × 10^{-3} – (9.92 ± 2.83) × 10^{-3} [b]
ten Kate et al. (2006)	UV, <6.5	(3.05 ± 0.87) × 10^{-5} [b]
Cottin et al. (2012), Noblet et al. (2012)	solar UV	(2.58 ± 0.39) × 10^{-2}
Bertrand et al. (2015)	solar UV	3.60 × 10^{-2}
Poch et al. (2013), Poch et al. (2014)	UV, 3.1–6.5	(4.14 ± 1.18) × 10^{-3} [b]
Kminek & Bada (2006)	γ, 1.17 × 10^6 and 1.33 × 10^6	0.39–4.23
Gerakines et al. (2012)	p^+, 8 × 10^5	3.5
Gerakines & Hudson (2013)	p^+, 8 × 10^5	28
Pilling et al. (2013)	p^+, 1 × 10^6	18 (α-glycine), 73.1 (β-glycine)
Gerakines & Hudson (2015)	p^+, 8 × 10^5	2.42
Maté et al. (2014)[a]	UV, 6.2–10.3 and e^-, 2 × 10^3	UV: 14.1 ± 8.8[b], e^-: (1.70 ± 0.05) × 10^5
Maté et al. (2015)[a]	e^-, 2 × 10^3	64.2 ± 2.0 (300 K), 128.3 ± 4.1 (90 K), 183.1 ± 5.8 (40 K)
Pilling et al. (2014)[a]	e^-, 2 × 10^3	(2.50 ± 0.08) × 10^3 (α-glycine, 300 K), (4.99 ± 0.16) × 10^3 (α-glycine, 14 K), (3.33 ± 0.11) × 10^3 (β-glycine, 300 and 14 K)

Notes.
[a] Doses determined by CASINO simulation using experimental data of the cited paper.
[b] Using destruction cross section determined by ten Kate et al. (2005).

effect on the decomposition rates and accelerate the decomposition through an active oxygen-initiated chemistry. Therefore, at least two separate mechanisms exist that degrade glycine in the presence of ClO_4^-: radiolysis by the electrons *and* oxidation of glycine (and possibly the fragments formed by the radiolysis) by the O atoms released from ClO_4^-, with each pathway (radiolysis vs. oxidation) contributing almost equally (Table 5). *Third*, the formation rates of CO_2 and CO suggest that the formation of both species is accelerated in the presence of ClO_4^- by a factor of between three and five (Table 5). This finding also proposes two separate mechanisms that degrade glycine in the presence of ClO_4^-: radiolysis by electrons and oxidation by reactive O atoms. *Fourth*, the degradation rates of pure glycine are significantly higher than the formation rates of CO_2 and CO. This suggests that, besides the decomposition via (R1), other hitherto-unidentified degradation pathways of glycine must exist by polymerization (Table 5). *Finally*, besides CO_2 and CO, three alternative products were identified tentatively via Reactions (R1)–(R3) to be CH_3NH_2, CH_4, and NH_3. These pathways can only account for 41% ± 20% and 32% ± 15% of the CO_2 and CO formed (Table 6). Therefore, additional oxidation pathways must exist to account for this discrepancy. Recall that the increase in glycine decomposition can be related to O atoms generated by the radiolysis of the ClO_4^-, providing a unique oxidizing environment in the radiolyzed samples.

Although the degradation of organics in the presence of oxidizers has been explored for over two decades, no coherent understanding has been achieved to date (Table 1). This is evident from the inconsistent product identification (or lack thereof), which is mainly restricted to CO_2 and CO. Further, the doses of the simulation experiments range from 10^{-5} eV per molecule to 10^5 eV per molecule, covering 10 orders of magnitude, with the latter exceeding the average dose of the organics exposed to GCRs in the upper 5–10 cm of the Martian soil (39 eV per molecule) by three orders of magnitude at least (Table 8). The current work represents the first systematic understanding toward quantitative concepts on the ClO_4^--assisted, radiation-induced decomposition of organics on the Martian surface. We provide temperature-dependent rate constants that can be exploited in future Martian surface models on the degradation of organics, and we also propose reaction products beyond the well-established CO_2 and CO species. In order to identify organic degradation products beyond any doubt, further experiments are necessary that incorporate alternative detection schemes of the organics.

Photoionization reflectron time-of-flight mass spectrometry (PI-ReTOF-MS), which records the temperature-dependent mass spectra upon photoionization of the subliming molecules with a single vacuum UV (VUV) light, represents an excellent choice (Jones & Kaiser 2013; Kaiser et al. 2014; Maity et al. 2014a, 2014b, 2015). Further, the effects of alternative oxidants such as iron and oxides could also accelerate the destruction of organics via heterogeneous catalysis as an alternative reaction pathway. There is laboratory evidence that goethite (α-FeOOH) and hematite (α-Fe_2O_3) can catalyze the decomposition of polyhydroxylated molecules (Shkrob & Chemerisov 2009; Shkrob et al. 2010), nucleic acids (Shkrob et al. 2011a), and carboxylic acids (Shkrob et al. 2011b). Moreover, measurements performed on Mars showed that iron-bearing phases might have a catalytic effect on the chlorination of benzene (Freissinet et al. 2015), which is similar to known methods of industrial chlorobenzene synthesis.

This work was supported by the National Aeronautics and Space Administration under Grant NNX14AG39G.

REFERENCES

Acuña, M. H., Connerney, J. E. P., Wasilewski, P., et al. 1998, Sci, 279, 1676
Armstrong, J. C., Leovy, C. B., & Quinn, T. 2004, Icar, 171, 255
Atreya, S. K., Wong, A.-S., Renno, N. O., et al. 2006, AsBio, 6, 439
Bennett, C. J., Ennis, C. P., & Kaiser, R. I. 2014, ApJ, 794, 57
Bennett, C. J., Jamieson, C., Mebel, A. M., & Kaiser, R. I. 2004, PCCP, 6, 735
Bennett, C. J., Jamieson, C. S., & Kaiser, R. I. 2009, PCCP, 11, 4210
Bennett, C. J., Jamieson, C. S., & Kaiser, R. I. 2010, PCCP, 12, 4032
Bennett, C. J., Jamieson, C. S., Osamura, Y., & Kaiser, R. I. 2005, ApJ, 624, 1097
Bennett, C. J., Jamieson, C. S., Osamura, Y., & Kaiser, R. I. 2006, ApJ, 653, 792
Bennett, C. J., & Kaiser, R. I. 2005, ApJ, 635, 1362
Bennett, C. J., & Kaiser, R. I. 2007, ApJ, 660, 1289
Bertrand, M., Chabin, A., Colas, C., et al. 2015, IJAsB, 14, 89
Biemann, K., & Bada, J. L. 2011, JGRE, 116, E12001
Biemann, K., Oró, J., Toulmin, P., et al. 1976, Sci, 194, 72
Bishop, J. L., Quinn, R., & Dyar, M. D. 2014, AmMin, 99, 1580
Bland, P., & Smith, T. 2000, Icar, 144, 21
Botta, O., & Bada, J. L. 2002, SGeo, 23, 411
Bullock, M. A., Stoker, C. R., McKay, C. P., & Zent, A. P. 1994, Icar, 107, 142
Carrier, B. L., & Kounaves, S. P. 2015, GeoRL, 42, 3739
Chevrier, V. F., Hanley, J., & Altheide, T. S. 2009, GeoRL, 36, L10202
Chowdhry, B. Z., Dines, T. J., Jabeen, S., & Withnall, R. 2008, JPCA, 112, 10333
Chun, S. F. S., Pang, K. D., Cutts, J. A., & Ajello, J. M. 1978, Natur, 274, 875
Cockell, C. S., & Raven, J. A. 2004, Icar, 169, 300
Cottin, H., Guan, Y. Y., Noblet, et al. 2012, AsBio, 12, 412
Davila, A. F., Willson, D., Coates, J. D., & McKay, C. P. 2013, IJAsB, 12, 321
Drouin, D., Couture, A. R., Joly, D., et al. 2007, Scanning, 29, 92
Encrenaz, T., Greathouse, T., Lefévre, F., & Atreya, S. 2012, P&SS, 68, 3
Flynn, G. J. 1996, EM&P, 72, 469
Flynn, G. J. 1997, in LPI Contrib. 916, I Workshop on Early Mars, ed. S. M. Clifford, A. H. Treiman, H. E. Newsom, & J. D. Farmer (Houston, TX: LPI), 33
Freissinet, C., Glavin, D. P., Mahaffy, P. R., et al. 2015, JGRE, 120, 495
Furić, K., Mohaček, V., Bonifačić, M., & Štefanić, I. 1992, JMoSt, 267, 39
Gerakines, P. A., Bray, J. J., Davis, A., & Richey, C. R. 2005, ApJ, 620, 1140
Gerakines, P. A., & Hudson, R. L. 2013, AsBio, 13, 647
Gerakines, P. A., & Hudson, R. L. 2015, Icar, 252, 466
Gerakines, P. A., Hudson, R. L., Moore, M. H., & Bell, J.-L. 2012, Icar, 220, 647
Gerakines, P. A., Schutte, W. A., Greenberg, J. M., & van Dishoeck, E. F. 1995, A&A, 296, 810
Hanley, J., Chevrier, V. F., Barrows, R. S., Swaffer, C., & Altheide, T. S. 2015, JGRE, 120, 1415
Hassler, D. M., Zeitlin, C., Wimmer-Schweingruber, R. F., et al. 2014, Sci, 343, 1244797
He, J., Gao, K., Vidali, G., Bennett, C. J., & Kaiser, R. I. 2010, ApJ, 721, 1656
Hecht, M. H., Kounaves, S. P., Quinn, R. C., et al. 2009, Sci, 325, 64
Holtom, P. D., Bennett, C. J., Osamura, Y., Mason, N. J., & Kaiser, R. I. 2005, ApJ, 626, 940
Houck, R. C. 1930, JAChS, 52, 2420
Hubbard, J. S., Hardy, J. P., & Horowitz, N. H. 1971, PNAS, 68, 574
Jackson, W. A., Davila, A. F., Sears, D. W. G., et al. 2015, E&PSL, 430, 470
Jones, B. M., & Kaiser, R. I. 2013, JPCL, 4, 1965
Kaiser, R. I., Maity, S., & Jones, B. M. 2014, PCCP, 16, 3399
Kaiser, R. I., Stockton, A. M., Kim, Y. S., Jensen, E. C., & Mathies, R. A. 2013, ApJ, 765, 111
Kayi, H., Kaiser, R. I., & Head, J. D. 2011, PCCP, 13, 15774
Kayi, H., Kaiser, R. I., & Head, J. D. 2012, PCCP, 14, 4942
Kim, Y. S., Wo, K. P., Maity, S., Atreya, S. K., & Kaiser, R. I. 2013, JAChS, 135, 4910
Kminek, G., & Bada, J. L. 2006, E&PSL, 245, 1
Kounaves, S. P., Chaniotakis, N. A., Chevrier, V. F., et al. 2014, Icar, 232, 226
Leshin, L. A., Mahaffy, P. R., Webster, C. R., et al. 2013, Sci, 341, 1238937
Lewis, J. M. T., Watson, J. S., Najorka, J., et al. 2015, AsBio, 15, 247
Lewis, R. J., Sr. (ed.) 2007, Hawley's Condensed Chemical Dictionary (15th ed.; Hoboken, NJ: Wiley), 779
Luna, R., Satorre, M. Á, Domingo, M., Millán, C., & Santonja, C. 2012, Icar, 221, 186
Luo, Y.-R. 2007, Comprehensive Handbook of Chemical Bond Energies (Boca Raton, Fl: CRC Press), 187
Maity, S., Kaiser, R. I., & Jones, B. M. 2014a, FaDi, 168, 485
Maity, S., Kaiser, R. I., & Jones, B. M. 2014b, ApJ, 789, 36
Maity, S., Kaiser, R. I., & Jones, B. M. 2015, PCCP, 17, 3081
Marion, G., Catling, D., Zahnle, K., & Claire, M. 2010, Icar, 207, 675
Maté, B., Rodriguez-Lazcano, Y., Galvez, O., Tanarro, I., & Escribano, R. 2011, PCCP, 13, 12268
Maté, B., Tanarro, I., Escribano, R., Moreno, M. A., & Herrero, V. J. 2015, ApJ, 806, 151
Maté, B., Tanarro, I., Moreno, M. A., et al. 2014, FaDi, 168, 267
Melnik, O., & Parrot, M. 1998, JGRA, 103, 29107
Miller, F. A., & Wilkins, C. H. 1952, AnaCh, 24, 1253
Mills, A. A. 1977, Natur, 268, 614
Ming, D. W., Lauer, H. V., Archer, P. D., et al. 2009, LPSC, 40, 2241
Moores, J. E., & Schuerger, A. C. 2012, JGRE, 117, E08008
Morton, R. J., & Kaiser, R. I. 2003, P&SS, 51, 365
Navarro-González, R., Vargas, E., de la Rosa, J., Raga, A. C., & McKay, C. P. 2010, JGRE, 115, E12010
Noblet, A., Stalport, F., Guan, Y. Y., et al. 2012, AsBio, 12, 436
Nuding, D., Rivera-Valentin, E., Davis, R., et al. 2014, Icar, 243, 420
Oró, J., & Holzer, G. 1979, JMolE, 14, 153
Oyama, V. I., & Berdahl, B. J. 1977, JGR, 82, 4669
Oyama, V. I., & Berdahl, B. J. 1979, JMolE, 14, 199
Pang, K. D., Chun, S. F. S., Ajello, J. M., Nansheng, Z., & Minji, L. 1982, Natur, 295, 43
Pavlov, A. A., Vasilyev, G., Ostryakov, V. M., Pavlov, A. K., & Mahaffy, P. 2012, GeoRL, 39, L13202
Pilling, S., Mendes, L. A. V., Bordalo, V., et al. 2013, AsBio, 13, 79
Pilling, S., Nair, B. G., Escobar, A., Fraser, H., & Mason, N. 2014, EPJD, 68, 58
Poch, O., Jaber, M., Stalport, F., et al. 2015, AsBio, 15, 221
Poch, O., Kaci, S., Stalport, F., Szopa, C., & Coll, P. 2014, Icar, 242, 50
Poch, O., Noblet, A., Stalport, F., et al. 2013, P&SS, 85, 188
Rosado, M. T., Duarte, M. L. T., & Fausto, R. 1998, VibSpectr, 16, 35
Shkrob, I. A., & Chemerisov, S. D. 2009, JPCC, 113, 17138
Shkrob, I. A., Chemerisov, S. D., & Marin, T. W. 2010, AsBio, 10, 425
Shkrob, I. A., Marin, T. W., Adhikary, A., & Sevilla, M. D. 2011a, JPCC, 115, 3393
Shkrob, I. A., Marin, T. W., Chemerisov, S. D., & Sevilla, M. D. 2011b, JPCC, 115, 4642
Smith, M. L., Claire, M. W., Catling, D. C., & Zahnle, K. J. 2014, Icar, 231, 51
Stoker, C. R., & Bullock, M. A. 1997, JGRE, 102, 10881
Sutter, B., Ming, D. W., Boynton, W. V., et al. 2009, LPICo, 1502, 29
ten Kate, I. L., Garry, J. R., Peeters, Z., Foing, B., & Ehrenfreund, P. 2006, P&SS, 54, 296
ten Kate, I. L., Garry, J. R. C., Peeters, Z., et al. 2005, M&PS, 40, 1185
Toner, J., Catling, D., & Light, B. 2014, GeCoA, 136, 142
Turner, A. M., Abplanalp, M. J., Chen, et al. 2015, PCCP, 17, 27281
Turner, A. M., Abplanalp, M. J., & Kaiser, R. I. 2016, ApJ, in press
Zheng, W., & Kaiser, R. I. 2007, CPL, 440, 229